



Numerical Simulation of the 3D Asymmetric Inner States of an Ironmaking Blast Furnace Resulting From Circumferential Non-uniform Burden Distribution

LULU JIAO, SHIBO KUANG, YUNTAO LI, XIAOMING MAO, HUI XU,
and AIBING YU

The circumferential uniformity of burden distribution is of critical importance in maintaining the stable and efficient operation of blast furnaces (BFs). It significantly affects the circumferential gas distribution and the reduction process of ferrous materials. However, during the burden-charging process at the furnace top, circumferential non-uniformity inevitably occurs, especially for bell-less top BFs with parallel hoppers. So far, few studies have been reported on the effects of non-uniform burden distribution on the 3D asymmetric inner states of BFs. In this work, the effects of circumferential non-uniform ore-to-coke ratio on the cohesive zone (CZ) shape and location, multiphase flow, thermochemical behaviors, and overall BF performance are numerically studied. This is based on a recently developed 3D computational fluid dynamics (CFD) process model, which features the 3D-layered burden structure and CZ, trickling liquid flow, particle size degradation, and stockline variation. The results show that the high-temperature reducing gas generated in raceways is re-distributed during its ascending process to the furnace top due to the circumferential non-uniform ore-to-coke ratio and, hence, the bed permeability, leading to the increasing temperatures in the low ore-to-coke region but the decreasing ones in the high ore-to-coke region. This asymmetric thermal state results in the 3D inclined CZ, which increases the non-uniformities in gas pressure, and liquid mass flow rate and temperature at the slag surface. In addition, both the sinter reduction degradation and the coke size reduction due to gasification intensify in the high ore-to-coke region but attenuate in the low ore-to-coke region, which increases the BF non-uniformity of bed permeability, and hence, on the multiphase flow and thermochemical behaviors. Moreover, with the increase of circumferential non-uniform degree of ore-to-coke ratio, the average top gas temperature and average tuyere gas pressure slightly increase; however, the average liquid outlet temperature slightly decreases. The model comprehensively illustrates the 3D asymmetric inner states and overall performance resulting from non-uniform burden distribution, which provides an effective tool for BF operation and control in practice.

<https://doi.org/10.1007/s11663-023-02722-7>

© The Minerals, Metals & Materials Society and ASM International 2023

I. INTRODUCTION

THE blast furnace (BF) still maintains its dominant role in the ironmaking process because of its high efficiency. So far, this process occupies around 63 percent of the total hot metal (HM) production for steelmaking in the world.^[1] In the operation of modern ironmaking BFs, the hot blast, usually oxygen enriched, is injected into the furnace at a high speed of over 200 m/s *via* the uniformly allocated tuyeres at the lower part of the furnace. Meanwhile, the ore and coke batches are alternatively charged into the furnace throat, forming stratified burden structure in the BF shaft. During the descending process of the solid phase, the ferrous materials are gradually heated, reduced, and melted by

LULU JIAO is with the School of Energy and Environment, Southeast University, Nanjing, 210096, P.R. China. Contact e-mail: lulu.jiao@simpas.cn SHIBO KUANG is with the Department of Chemical and Biological Engineering, Monash University, Melbourne, VIC 3800, Australia. YUNTAO LI and XIAOMING MAO are with the Ironmaking Division, Research Institute (R&D Center), Baoshan Iron & Steel Co., Ltd, Shanghai 201900, P.R. China. HUI XU is with the Ironmaking Plant, Baoshan Iron & Steel Co., Ltd, Shanghai 201900, P.R. China. AIBING YU is with the School of Energy and Environment, Southeast University and also with the Department of Chemical and Biological Engineering, Monash University. Contact e-mail: aibing.yu@monash.edu

Manuscript submitted February 17, 2022; accepted January 7, 2023.

Article published online February 14, 2023.

the ascending reducing gas. The alternative layered burden structure of ore and coke particles remains until the cohesive zone (CZ), where the ferrous materials experience softening and melting. Therefore, the BF is substantially a counter-current moving bed reactor that involves multiphase flow, heat and mass transfer, and chemical reactions of gas, solid, and liquid phases. It has been accepted that the layered burden structure inside a BF primarily determines the ascending gas flow, gas–solid heat exchange, and thus, plays a vital role in affecting the BF global performance, including process efficiency and stability.^[1,2] Therefore, the burden distribution at the furnace throat, specifically referred to the radial and circumferential distributions of the ore and coke sizes and the ore-to-coke ratio, are of significant importance to BF operation.

In modern ironmaking BFs, the burden distribution is often adjusted and controlled *via* the bell-less charging system, which is usually equipped with a rotating chute and two parallel hoppers. Various numerical and experimental efforts have been made to better control the burden-charging process.^[3] For instance, the popular discrete element method (DEM) has been widely used to study various phenomena in the burden-charging process, such as particle flow and segregation in the hopper,^[4] particle flow on the chute,^[5] burden descending in the BF,^[6] and collapse of the coke layer, *etc.*,^[7] However, the previous studies of burden distribution were mainly confined under cold conditions. Some studies also considered the effects of burden distribution on the inner states and global performance of BF but focused on the radial distribution. For example, Li *et al.*^[8] found that a uniform radial ore-to-coke ratio has the highest top gas utilization factor and the lowest coke rate; however, it has a long horizontal CZ, leading to the largest gas pressure drop and significant fluctuation of inner states. Differently, the center-developed burden distribution, namely more coke particles, is charged into the furnace center, can prevent the inactivation of the lower furnace,^[9] avoids the discontinuous solid flow,^[10] and realizes a stable operation, therefore, has been widely used in the industrial BFs. Some researchers also numerically or experimentally investigated the effect of substituting the expensive coke with some novel burden materials to improve the BF efficiency, such as carbon composite briquette (CCB), hot briquetted iron (HBI) and nut coke, *etc.*,^[11–16] These studies regarding burden distribution provide meaningful guides for improving the process efficiency and stability. However, another important factor that affects the BF running efficiency, namely the circumferential imbalance of burden distribution, has not attracted too much attention.

The circumferential non-uniform burden distribution inevitably occurs because of the inherent properties of bell-less top charging system. When the burden materials flow out from the parallel hoppers, the particles do not flow along the center of the feeder spout, but flow along its wall at the opposite side of the charging hopper, and as the chute rotates, the colliding points of the eccentric flow on the chute form an oval-shaped

trajectory, which leads to the variation of retention time on the chute and, thus, the non-uniformity of burden distribution along the circumference.^[17] The circumferential non-uniformity can also be affected by the non-uniform transient mass discharge rate of coke/ore particles from the parallel hoppers.^[18,19] The circumferential imbalance of burden distribution has been theoretically or numerically investigated by various researchers in terms of the circumferential falling point and mass flow rate.^[20–25] Results show that the maximum deviation of circumferential mass flow rate could be up to 10 pct of its average value.^[22] In addition to this, the influence of chute shape, chute rotating speed, and chute tilting angles on the circumferential distribution has been systematically investigated.^[23] Although people have realized that changing the rotation direction of the chute and the alternative use of ore and coke hopper are effective means to eliminate the non-uniformity of burden distribution in the circumferential direction,^[24] in the actual operation of BF, this non-uniform phenomenon cannot be completely eliminated due to the complexity of process control. Therefore, it is essential to study the effect of non-uniform burden distribution on the 3D asymmetric inner states of BF. However, at the current stage, this understanding is very limited, especially on quantitative analysis.

The BFs are operated under extreme complicated conditions coupled with extensive momentum, heat, and mass transfer of gas, solid, and liquid phases. It is difficult and expensive to study by the experimental method or plant studies.^[26] The theoretical analysis, based on overall heat and mass balance, and *in-situ* measurement are cheap and easy to be implemented, but do not have access to the BF inner states. Alternatively, the shortcomings of the above-mentioned methods can be overcome by the method of simulation and modeling, which has gradually become a promising approach and been widely used in the revealing of complex BF inner states and in the BF process design and control. During the past few decades, consistent efforts have been made to the development and applications of BF models, including both the continuum method and the discrete method regarding the treatment of solid phase, as reviewed by different researchers.^[27–32] In summary, the BF models can be divided into four categories based on the simulation regions, including the raceway flow and combustion model,^[33–36] hearth flow and heat transfer model,^[37–41] burden distribution model,^[42–44] and BF process model.^[45–55] In this work, a 3D BF process model that calculates the region from the stockline to the slag surface at the 3D industrial scale, is needed. At the current stage of BF process model development, most models are 2D and only a few 3D models were reported.^[47,48,54] Here, the one recently developed by Jiao *et al.*^[56,57] is adopted, which considers some key features of BF, including 3D-layered burden structure and CZ, trickling liquid flow, particle size degradation, and stockline variation. However, these features are neglected in the other 3D BF process models.^[47,48,54] The detailed model description could be

found in the next section.

In this work, the 3D multiphase flow and thermochemical behaviors under circumferential non-uniform burden distribution are studied using the recent 3D BF process model.^[56,57] The asymmetric characteristic of inner states are analyzed in detail in terms of the burden layer structure, cohesive zone, gas velocity and pressure, solid temperature, liquid mass flow rate and temperature, iron ore reduction degree, and particle size degradation. This analysis helps better understand the effect of non-uniform burden distribution so that potential problems can be better identified.

II. MODEL DESCRIPTION

A. Model Framework

The current work is based on the 3D BF process model recently developed by Jiao *et al.*^[56,57] This model is a steady-state multi-fluid model based on CFD. It calculates the region from the slag surface in the hearth up to the stockline in the throat. Table I summarizes the governing equations of the present model. The gas, solid (*i.e.*, burden materials), and liquid (*i.e.*, HM and slag) phases considered in this model are all treated as interpenetrating continua. The powder phase (*i.e.*, pulverized coal) is considered through the heat and

mass balance in front of the tuyeres. However, the powder flow sub-model is not explicitly established at the current stage of model development. This treatment is acceptable because the gas, solid, and liquid phases dominate the BF performance when the pulverized coal injection (PCI) rate is relatively low. Each considered phase consists of one or more components, and each component has its composition and physical properties. These phases are described, respectively, by the separate conservation equations of mass, momentum, and enthalpy, with key chemical reactions considered.

The gas flow is simulated by the well-established volume averaged Navier-Stokes equation. The gas inlet dimension is set according to the real tuyere size of the actual BF, with the velocity inlet boundary condition adopted. The raceway region, generated by the violent collision and combustion of high-speed blast and coke bed, is a preset cavity with its profile determined by DEM simulations and with its dimension determined according to the data provided by our industrial collaborators. Ideally, the voidage in the raceway is set as 1.0. It is assumed that the coke and pulverized coal are fully combusted with the oxidizer in the blast, and completely forms the reducing gas, including CO and H₂. The specific composition, temperature, and mass flow rate of the reducing gas are determined according to the local mass and heat balance in the raceway for given conditions of hot blast and coal/coke properties, which are used as the gas inlet conditions in simulations, as done by the other BF process models.^[45,49,50,52,55] In other words, the combustion inside raceways is not explicitly considered here. However, the effects of raceway boundaries on surrounding gas and liquid flows and the associated transport phenomena are taken into account. The gas temperature and compositions of CO, CO₂, H₂, H₂O, and N₂ are all solved by the general convection-diffusion equation, with chemical reactions as the source terms.

The solid phase is composed of iron ore, coke, and flux particles, forming layered structures in the shaft. However, in the calculation of solid flow, the solid phase is treated as a mixture of three type solid particles, with the solid density and volume fraction determined according to the mass ratio of different materials. The governing equation is the modification of the viscous model proposed by Zhang *et al.*,^[58] with the rate-independent stress neglected. This simplification has been proved to be effective to capture the key flow characteristics of solids in BFs, and has the advantage to be directly implemented into a comprehensive BF process model.^[59] In the calculation, the burden materials in the BF throat move downward with an identical velocity. The number of solid outlets is equal to the number of active tuyeres in the calculation domain, and the split ratio at each solid outlet is determined according to the blast rate at the corresponding tuyere, since the injected oxygen is assumed to be fully combusted with the descending coke. In addition, the iterative method to determine the stagnant zone profile proposed by Zhang *et al.*^[58] is straightforwardly extended to 3D calculation. The alternative stratified structure of ore and coke batches is determined by the solid timelines, batch

Table I. Governing Equations of the 3D BF Process Model

Items	Descriptions
Mass Conservation	$\nabla \cdot (\varepsilon_i \rho_i \mathbf{u}_i) = S_i$, where $S_i = -\sum_k (\beta_{i,k} R_k^*)$
Momentum Conservation	
Gas	$\nabla \cdot (\varepsilon_g \rho_g \mathbf{u}_g \mathbf{u}_g) = \nabla \cdot \boldsymbol{\tau}_g - \varepsilon_g \nabla p + \varepsilon_g \rho_g \mathbf{g} + \mathbf{F}_g^s$ $\boldsymbol{\tau}_g = \varepsilon_g \mu_g [\nabla \mathbf{u}_g + (\nabla \mathbf{u}_g)^T] - \frac{2}{3} \varepsilon_g \mu_g (\nabla \cdot \mathbf{u}_g) \mathbf{I}$
Solid	$\nabla \cdot (\varepsilon_s \rho_s \mathbf{u}_s \mathbf{u}_s) = \nabla \cdot \boldsymbol{\tau}_s - \varepsilon_s \nabla p_s + \varepsilon_s \rho_s \mathbf{g}$ $\boldsymbol{\tau}_s = \varepsilon_s \mu_s [\nabla \mathbf{u}_s + (\nabla \mathbf{u}_s)^T] - \frac{2}{3} \varepsilon_s \mu_s (\nabla \cdot \mathbf{u}_s) \mathbf{I}$
Liquid	$\mathbf{F}_{l,d}^g + \mathbf{F}_{l,d}^s + \mathbf{F}_{l,d}^{\text{gravity}} = 0$
Heat and Species Conservation	$\nabla \cdot (\varepsilon_i \rho_i \mathbf{u}_i \varphi_{i,m}) - \nabla \cdot (\varepsilon_i \Gamma_i \nabla \varphi_{i,m}) = S_{\varphi_{i,m}}$ if $\varphi_{i,m}$ is $H_{i,m}$, $\Gamma_i = k_i / c_{p,i}$ $S_{\varphi_{i,m}} = \delta_i h_{ij} \alpha (T_i - T_j) + \eta_i \sum_k R_k^* (-\Delta H_k)$ if $\varphi_{i,m}$ is $\omega_{i,m}$, $\Gamma_i = \rho_i D_i$, $S_{\varphi_{i,m}} = \sum_k \alpha_{i,m,k} R_k^*$ where $\varphi_{i,m} = \omega_{g,CO}, \omega_{g,CO_2}, \omega_{g,H_2}, \omega_{g,H_2O}, \omega_{g,N_2},$ $\omega_{s,Fe_2O_3}, \omega_{s,Fe_3O_4}, \omega_{s,FeO}, \omega_{s,flux}$
Phase Volume Fraction	$\sum_i \varepsilon_i = 1$
State Equation	$p = \rho_g R T_g / \sum_i (y_i M_i)$
Timeline Equation	$\nabla \cdot (\rho_{bulk} \mathbf{u}_s t_s) = \rho_{bulk}$

weight, and the ore-to-coke ratio distribution. The solid timeline equation is shown in Table I. The simulation of CZ follows the treatment in Dong *et al.*'s model,^[49] where the ore particle size and voidage in the CZ are functions of the ore shrinkage ratio. The solid temperature and mass fractions of the various components contained in the ferrous materials are solved by the general convection-diffusion equation. In order to predict the gas permeability more realistically, the coke size reduction due to gasification and sinter size reduction due to low-temperature reduction degradation are also considered here.^[60]

The liquid phase in BF consists of liquid iron, namely HM and slag. For simplification, the liquid is treated as a mixture of the HM and slag, with the liquid properties calculated by the overall mass-weighted averages of two liquids. The respective mass fractions of HM and slag are determined by the global HM rate and slag rate. Even though the trickling flow features can be described by the moving particle semi-implicit (MPS) method and smooth-particle hydrodynamics (SPH) method, the high computational demand makes it impossible to be implemented in a BF process model.^[61,62] For this reason, the force balance model is adopted here, which describes the liquid flow as rivulets or droplets under the combined effects of gravity, gas drag, and bed resistance. In addition, the stochastic model is adopted to account for the dispersion effect of the liquid flow resulting from the complicated pore structures of the coke bed. With the combination of force balance model and stochastic model, the trickling liquid flow features at

the furnace lower part are simulated at the industrial scale. The detailed description of the liquid flow model can be found elsewhere.^[56,57] The liquid temperature is also solved by the general convection-diffusion equation.

B. Momentum, Mass, and Heat Transfer and Chemical Reactions

Intensive momentum, mass, and heat transfer and chemical reactions occur inside the blast furnace. Table II describes interaction forces between phases and the transport coefficients in the present model. Ergun's equation^[63] is employed to describe the gas-solid interaction as reducing gas flows through a packed bed. The gas drag force exerted on liquid droplet and the bed resistance on liquid droplet are described by the formulations of Wang *et al.*^[64] The effective gas diffusion coefficient is determined by the relationship between Peclet number and Reynolds number.^[2] The diffusion coefficients of solid and liquid phases are ignored. The effective gas heat conductivity is determined by $k_{gn} = c_p \rho D_{gn}^e$.^[2] The effective solid heat conductivity k_{sc}^e is the effective heat conductivity caused by the conduction between particles and the radiation between non-contacting particles.^[2] The effective liquid heat conductivities k_l are determined according to the data from the literature.^[45] The gas-solid convection heat transfer coefficient h_{gs} is calculated using the Ranz-Marshall equation, modified by Akiyama for the use in moving beds.^[65,66] The gas-liquid heat transfer

Table II. Interphase Interaction Forces and Transport Coefficients in the Present Model

Items	Formulations
Interaction Forces	
Gas-Solid ^[63]	$\mathbf{F}_g^s = \left[150 \frac{\mu_g \varepsilon_s^2}{\varepsilon_g d_s^2} + 1.75 \frac{\varepsilon_s \rho_g}{d_s} \mathbf{u}_s - \mathbf{u}_g \right] (\mathbf{u}_s - \mathbf{u}_g)$
Liquid-Gas ^[64]	$\mathbf{F}_{l,d}^g = \frac{1}{2} C_{DG} A_{g-1} \rho_g \mathbf{U}_g - \bar{\mathbf{U}}_1 (\mathbf{U}_g - \bar{\mathbf{U}}_1)$
Liquid-Solid ^[64]	$\mathbf{F}_{l,d}^s = \frac{1}{2} C_{DS} A_{s-1} \rho_1 \bar{\mathbf{U}}_1 \bar{\mathbf{U}}_1$
Gas Diffusion Coefficients ^[2]	$Re_g \geq 8; Pe_{g,rad} = 8, Pe_{g,axis} = 2.0$ $Re_g < 8; Pe_{g,rad} = Re_g, Pe_{g,axis} = 0.25 Re_g$
Conductivity	
Gas ^[2]	$k_{gn} = c_p \rho D_{gn}^e$
Solid ^[2]	$k_{sc}^e = (1 - \varepsilon_g) / (1/k_s + 1/k_s^e) + \varepsilon_g k_s^e$ and $k_s^e = 2.29 \times 10^{-7} d_s T_s^3$
Liquid ^[45]	$k_l = 0.0158 T_1$ for HM $k_l = 0.57$ for slag
Heat Transfer Coefficients	
Gas-Solid ^[46]	$h_{gs} = k_g / d_s \left(2.0 + 0.39 Re_{gs}^{0.5} Pr_g^{0.333} \right)$ and $Pr_g = c_{pg} \mu_g / k_g$
Gas-Liquid ^[45]	$E_{gl} = 4.18 \times 10^{-4} \varepsilon_g \rho_g u_g c_{pg} (\varepsilon_l \rho_l u_l)^{0.35} Re_{gl}^{-0.37} \cdot (Sc_g / Pr_g)^{0.667} (T_1 - T_g)$
Solid-Liquid ^[46]	$h_{sl} = 1 / (1/h_s + 1/h_l), h_s = 2 \sqrt{k_s c_{ps} \rho_s \tilde{u}_1 - \tilde{u}_s / \pi d_s}$ $h_l = 2 \frac{k_l}{d_s} \sqrt{Re_{sl} Pr_1} / (1.55 \sqrt{Pr_1} + 3.09 \sqrt{0.372 - 0.15 Pr_1})$ where, $Re_{sl} = \phi_s d_s \rho_1 \tilde{u}_1 - \tilde{u}_s / \mu_1$ and $Pr_1 = c_{p1} \mu_1 / k_1$

Table III. Chemical Reactions Considered in the Present Model

Items	Formulations
$\text{Fe}_2\text{O}_3(\text{s}) + \text{CO}(\text{g}) \rightarrow \text{Fe}(\text{s}) + \text{CO}_2(\text{g})$ ^[72]	$R_1^* = \frac{12\xi_{\text{ore}}\epsilon_{\text{ore}}P(y_{\text{CO}} - y_{\text{CO}}^c)/(8.314T_s)}{d_{\text{ore}}^2/D_{\text{g,CO}}^c[(1-f_o)^{-1/3}-1] + d_{\text{ore}}[k_1(1+1/K_1)]^{-1}}$
$\text{FeO}(\text{l}) + \text{C}(\text{s}) \rightarrow \text{Fe}(\text{l}) + \text{CO}(\text{g})$ ^[2]	$R_2^* = k_2(A_c/V_B)a_{\text{FeO}}$
$\text{C}(\text{s}) + \text{CO}_2(\text{g}) \rightarrow 2\text{CO}(\text{g})$ ^[72]	$R_3^* = \frac{6\xi_{\text{coke}}\epsilon_{\text{coke}}P y_{\text{CO}_2}/(8.314T_s)}{d_{\text{coke}}/k_1 + 6/(\rho_{\text{coke}}E_1k_3)}$
$\text{FeO}(\text{s}) \rightarrow \text{FeO}(\text{l})$ ^[46]	$R_4^* = \left\langle \frac{T_i - T_{\text{min,sm}}}{T_{\text{max,sm}} - T_{\text{min,sm}}} \right\rangle_0 \frac{\int \omega_{\text{sm}} \mathbf{u}_i \rho_i \epsilon_i dA}{M_{\text{sm}} \text{Vol}_{\text{cell}}}$
Flux _(s) → Slag _(l)	
$\text{Fe}_2\text{O}_3(\text{s}) + \text{H}_2(\text{g}) \rightarrow \text{Fe}(\text{s}) + \text{H}_2\text{O}(\text{g})$ ^[2]	$R_5^* = \frac{\pi d_{\text{ore}}^2 \phi_{\text{ore}}^{-1} N_{\text{ore}} \cdot 273 \cdot P (y_{\text{H}_2} - y_{\text{H}_2}^+) / (22.4 T_{\text{solid}})}{1/k_{15} + (d_{\text{ore}}/2)[(1-f_o)^{-1/3}-1] / D_{s5} + [(1-f_o)^{2/3}k_5(1+1/K_5)]^{-1}}$
$\text{C}(\text{s}) + \text{H}_2\text{O}(\text{g}) \rightarrow \text{CO}(\text{g}) + \text{H}_2(\text{g})$ ^[2]	$R_6^* = \frac{\pi d_{\text{coke}}^2 \phi_{\text{coke}}^{-1} N_{\text{coke}} \cdot 273 \cdot P y_{\text{H}_2} / 22.4 T_s}{1/k_{16} + 6/d_{\text{coke}}\rho_{\text{coke}}E_1k_6}$
$\text{CO}(\text{g}) + \text{H}_2\text{O}(\text{g}) \rightarrow \text{CO}_2(\text{g}) + \text{H}_2(\text{g})$ ^[2]	$R_7^* = 7.29 \times 10^{11} (y_{\text{CO}})^{1/2} (y_{\text{H}_2\text{O}}) (P/T_{\text{gas}})^{3/2} \epsilon \frac{\exp(-67300/RT_{\text{gas}})}{\sqrt{1 + 14.158 y_{\text{H}_2} P T_{\text{gas}}}} - 1.386 \times 10^{10} (y_{\text{CO}_2}) (y_{\text{H}_2})^{1/2} (P/T_{\text{gas}})^{3/2} \epsilon \frac{\exp(-57000/RT_{\text{gas}})}{\sqrt{1 + 4.24 y_{\text{CO}} P T_{\text{gas}}}}$
$\text{SiO}_2(\text{l}) + 2\text{C} \rightarrow \text{Si} + 2\text{CO}(\text{g})$ ^[2]	
$\text{SiO}_2(\text{l}) + 2\text{C}(\text{l}) \rightarrow \text{Si}(\text{l}) + 2\text{CO}(\text{g})$	$R_8^* = k_8(A_c/V_B)C_{\text{SiO}_2}; k_8 = 7.59 \times 10^4 \exp(-62870/RT_s)$

source E_{gl} is calculated by Mackey and Warner’s correlation for liquid metals trickling through packed beds.^[67] The solid–liquid heat transfer coefficient h_{sl} is derived by considering the resistances to heat transfer in both the interfacial boundary layer on the liquid side and the conductive resistance on the solid side, expressed as $h_{\text{sl}} = 1/(1/h_s + 1/h_l)$.^[46] For the wall boundary condition, the heat transfer can be expressed using Newton’s Law of Cooling. Based on the assumed refractory materials, the heat conduction coefficient of the furnace wall is expressed as $5 \text{ W} \cdot \text{m}^{-1} \cdot \text{K}^{-1}$.^[49] The chemical reactions considered in the present model are summarized in Table III.

C. Numerical Solution

An in-house Fortran F90 code is developed to solve the conservation equations (see Table I) based on the Finite Volume Method (FVM). The calculation domain is divided into structured hexahedral cells with all variables defined in the center of calculation cells. Rhie-Chow interpolation^[68] is applied to avoid checkerboard pressure–velocity decoupling. The SIMPLE algorithm^[69] is used to couple velocity and pressure of continuous phases. The liquid flow rate calculation is also under the framework of FVM, with the coefficient matrix determined by the force balance model and stochastic model.

Figure 1(b) illustrates the sequential solution procedure to calculate the coupled momentum, heat and mass transfer, and chemical reactions of gas, solid, and liquid phases. First, the gas input conditions in the simulation are determined according to the global heat and mass balance under given material and operational conditions in front of the tuyeres; Second, the raceway profile is determined and the solid outlets are identified; Third, the deadman profile and layered burden structure are

determined according to the timelines of solid flow; Fourthly, the approximate convergence results of flow, temperature, and concentration fields of gas and solid phases without the identification of CZ are calculated; Fifthly, with the determination of CZ, further the liquid phase is considered and the coupled thermochemical behaviors of gas, solid, and liquid phases are re-calculated, which are repeated until the CZ position converges. The CZ position is characterized by the volume ratio of lumpy zone and dripping zone. The solution is converged only when the difference of the ratios in two consecutive iterations is less than a specific value, which is set to 0.1 pct in this work.

Another important consideration for solution convergence is productivity. It is established that productivity is one of the key process parameters. It varies related to stockline variation and is dependent on the material, geometrical, and operational conditions. Corresponding to practical BF operations, productivity is treated as an output in the current model rather than as an input as in most previous models. To this effect, the burden charge rate is automatically adjusted according to the carbon balance illustrated in Figure 1(a) to adapt to given BF conditions for achieving specific in-furnace states. This way is like the consideration of stockline variation. For a converged solution, the difference between the coke combusted in raceways and the coke following into the raceway is $< 0.1 \text{ kg/tHM}$ to meet the coke balance requirement, as shown in Figure 1(b).^[53]

In the calculation of this 3D BF process model, the computational load dramatically increases due to the exponentially increasing CFD cell number from 2D to 3D. For example, a 5000-m³ industrial blast furnace can be divided into around 10 million hexahedral cells with the average cell size setting as $8 \text{ cm} \times 8 \text{ cm} \times 8 \text{ cm}$. The calculation is almost impossible to be achieved *via* the serial computing because of the limitation of

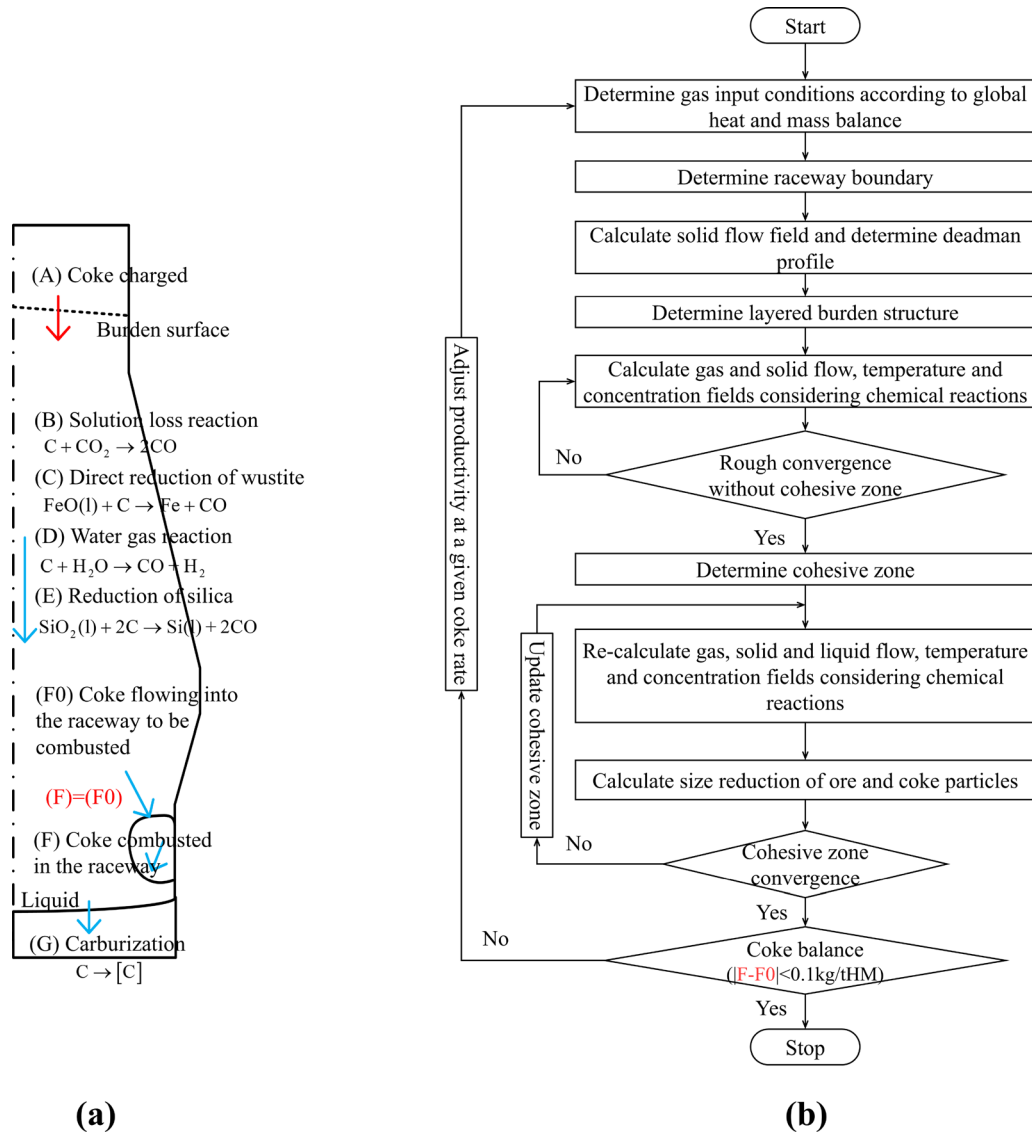


Fig. 1—Schematic illustration of (a) the coke balance in a BF and (b) solution procedure of the current 3D BF process model.

computational memory or the limitation of calculation time, which can even take a few months to obtain the results. As a result, the parallelization technology is required here. This is achieved based on the open-source parallel structured FVM single-phase CFD code *CAF-FA3D*,^[70] where the message passing interface (MPI) technology is adopted. This in-house code shows excellent parallel efficiency. The parallel calculation breaks through the technique bottleneck to study the 3D asymmetric characteristics at the 360 deg full scale, with more detailed internal information reflected when compared with the other reported 3D BF process models.^[47,48,54]

D. Simulation and Boundary Conditions

In this work, the effects of circumferential non-uniform burden distribution on the 3D asymmetric BF inner states are quantified using a 5000-m³ industrial BF. This BF is simulated at the actual scale. The working height of this BF can reach around 30 m. The hearth diameter is 14.5 m, with 40 tuyeres uniformly allocated along the hearth circumference. In the current simulation, in order to reduce the computational cost, half of the furnace, namely 180 deg and 20 tuyeres, is simulated, with the vertical cross-section setting as the symmetry boundary. The details of inlet, outlet, and wall boundary conditions for gas, solid, and liquid phases are shown in Table IV. The computational

Table IV. Boundary Conditions of the Present Model

	Inlet	Outlet	Wall
Gas Momentum	velocity inlet	zero gradient	no-slip condition
Gas Temperature	fixed temperature	zero gradient	Newton's Law of Cooling
Gas Concentration	fixed concentration	zero gradient	zero flux
Solid Momentum	velocity inlet	zero gradient	slip condition
Solid Temperature	fixed temperature	zero gradient	Newton's Law of Cooling
Solid Concentration	fixed concentration	zero gradient	zero flux
Liquid Temperature	—	zero gradient	Newton's Law of Cooling

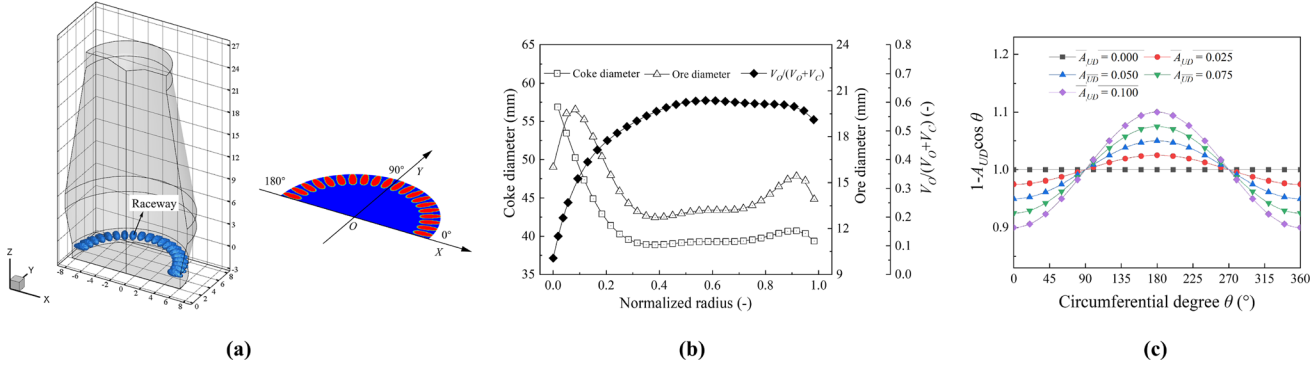


Fig. 2—Computational domain (a) and burden distribution at the furnace top [(b) radial distributions of ore and coke particle sizes and ore-to-coke ratio, and (c) circumferential variations of ore-to-coke ratio at different A_{UD} values].

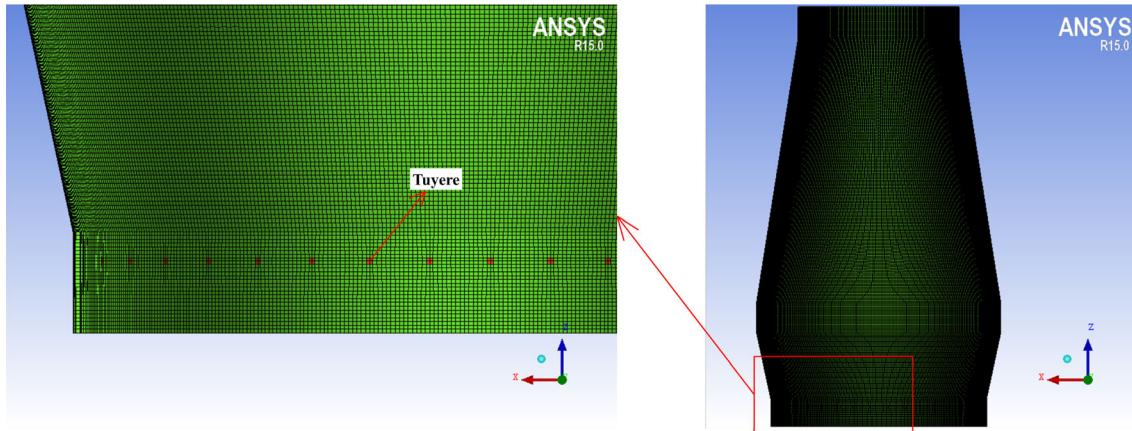


Fig. 3—Grid arrangements of the computational domain.

domain in Figure 2(a) is divided into around 5 million hexahedral CFD cells by the commercial software ANSYS, as can be seen in Figure 3. Since the mesh format is different from that of *CAFFA3D*,^[70] we have developed an in-house code to complete the mesh format transformation. The tuyere shape is simplified to be square to reduce the cell number.

The burden distribution, which refers to the spatial distributions of ore and coke particle sizes, and ore-to-coke ratio, is the model input in the BF throat. The ore-to-coke ratio $R_{O/(O+C)}$ is defined as the ratio of ore bulk volume to the addition of that of ore and coke, and expressed as follows:

$$R_{O/(O+C)} = V_O / (V_O + V_C). \quad [1]$$

Because of the wide range distribution of particle size in actual operation and the complicated effects of particle interpenetration on bed permeability, the effects of circumferential non-uniform ore-to-coke ratio on BF inner states are initially studied in this work. The spatial distribution of the ore-to-coke ratio in BF throat is described by the following equation:

$$R_{O/(O+C)}(r, \theta) = R_{O/(O+C),0}(r) \cdot (1 - A_{UD} \cos \theta), \quad [2]$$

where r is the furnace radius, θ is the circumferential azimuth degree and varies from 0 to 180 deg, as can be seen in Figure 2(a), $R_{O/(O+C)}(r, \theta)$ is the 2D spatial distributions of ore-to-coke ratio at the stockline surface, namely in both the radial and circumferential directions, $R_{O/(O+C)}(r)$ is the radial ore-to-coke distribution [see Figure 2(b)], A_{UD} is the circumferential non-uniform degree of ore-to-coke ratio. It can be seen from Figure 2(b) that more coke particles are charged into the furnace center, leading to the development of central gas flow. This information comes from our industrial collaborators, who obtained it from DEM simulations under the actual charging conditions.^[57] According to the previous findings,^[20-25] the burden mass flow rate usually presents the sine/cosine like distribution along the circumference. As a result, in the current simulation, $(1 - A_{UD} \cos \theta)$ is used to describe the circumferential variations of ore-to-coke ratio, as shown in Figure 2(c). In each simulation case, A_{UD} is the only independent variable, which varies from 0.00 to 0.10 with a constant interval of 0.025. The corresponding BF inner states and global performance indicators are analyzed. Larger A_{UD} indicates ore-to-coke ratio is more non-uniform along the circumference. $A_{UD} = 0$ corresponds to the uniform ore-to-coke ratio distribution. For simulation cases of $A_{UD} > 0$, it is clear from Figure 2(c) that 0 to 90 deg is the low ore-to-coke region, where less ore particles and more coke particles are placed; conversely, 90 to 180 deg is the high ore-to-coke region, where more ore particles and less coke particles are placed. Due to the smaller

diameter of ore particles [see Figure 2(b)], the low ore-to-coke region has better gas permeability and the high ore-to-coke region has worse gas permeability. In the following discussions, the term “low ore-to-coke region” is specifically referred to the 0 to 90 deg region, and “high ore-to-coke region” is specifically referred to the 90 to 180 deg region. Term “uniform/non-uniform burden distribution” is specifically referred to the circumferential uniform/non-uniform distribution of ore-to-coke ratio. Because of the symmetry of the circumferential variation between the low ore-to-coke region and high ore-to-coke region [see Figure 2(c)], the coke rate is automatically kept constant in all the simulation cases of this work.

In addition to the burden distribution, Table V lists the other constant operational conditions of the simulated BF in the current study, including the gas phase, solid phase, and powder phase. These conditions are the model inputs of the current BF process model. The gas inlet mass flow rate is the summarized value of the 20 tuyeres in the computational domain, which is assumed to be uniformly distributed among the tuyeres. This assumption is consistent with practical operations where the value opening in front of each tuyere is adjusted to ensure the uniform gas flow. The gas composition and temperature are also assumed uniform in the simulation. The charging/injection rate of the iron ore, coke, flux, and pulverized coal, as well as their corresponding components, are also listed. The charged iron ore mainly consists of sinter. The reduction degradation index (RDI) of sinter particles is assumed as 15 under the JIS RDI test. With this RDI value, the sinter reduction

Table V. Operational Conditions of the Simulated BF in the Current Study

Variables	Values
Gas Phase	
Inlet Mass Flow Rate, kg/s	94.07
Inlet Gas Components, Volume Fraction	CO 0.36872; CO ₂ 0.0; H ₂ 0.04634; H ₂ O 0.0; N ₂ 0.58494
Inlet Gas Temperature, K (°C)	2512 (2239)
Top Pressure, kPa	235
Solid phase	
Ore, t/tHM	1.593
Ore Components, Mass Fraction	Fe ₂ O ₃ 0.7975; FeO 0.0533; CaO 0.067; MgO 0.0093; SiO ₂ 0.0334; Al ₂ O ₃ 0.0110; MnO 0.0185; P ₂ O ₅ 0.0098
Average ore Particle size, m	0.013
Batch Weight of Iron Ore, t	140
RDI Value of Iron Ore	15
Circumferential Non-uniform Degree of Ore-to-Coke Ratio	0.000, 0.025, 0.050, 0.075, 0.100
Coke, kg/tHM	300
Coke Components, Mass Fraction	C 0.8704; SiO ₂ 0.0608; Al ₂ O ₃ 0.0418; CaO 0.0040; MgO 0.00024
Average Coke Particle Size, m	0.04
Flux, t/tHM	0.0178
Flux Components, Mass Fraction	CaO 0.0; MgO 0.0; SiO ₂ 1.0; Al ₂ O ₃ 0.0; CO ₂ in CaO 0.0; CO ₂ in MgO 0.0
Ore Voidage	$0.403(100d_{ore})^{0.14}$
Coke Voidage	$0.153 \log d_{coke} + 0.742$
Burden Temperature, K (°C)	298 (25)
Powder Phase	
Pulverized coal, kg/tHM	185
Coal Components, Mass Fraction	C 0.8169; H 0.0351; N 0.0112; S 0.0035; Ash 0.0754

degradation and the coke size reduction due to gasification are considered simultaneously, as done in our previous work.^[60]

In each simulation case, the solid inlet velocity is initially determined according to the burden distribution, coke/ore density, and a temporary productivity. During the iterative solution, the solid inlet velocity is automatically adjusted according to the coke mass balance in raceway, which predicts the final value of productivity under the given operational conditions. Meanwhile, the other overall performance indicators, such as the top gas temperature, top gas utilization factor, liquid temperature, *etc.*, and the BF inner states, represented by the CZ shape and location, multiphase flow and thermochemical behaviors, are also obtained. The simulation is carried out on our internal HPC platform, which is equipped with 64 Intel® Xeon® Processors E5-2680 v4, and each processor has 14 CPU cores. In this work, each simulation case is assigned with 10 Processors, and lasts for up to 72 hours to obtain the converged results.

III. RESULTS AND DISCUSSION

A. Model Validation

It should be pointed out that the 3D BF process model^[56,57] used in this work has been validated *via* different applications in our previous studies. First, the model validity has been examined by simulating an 9-m³ experimental BF,^[26] which shows reasonable agreement between the measured and predicted global performance indicators such as the productivity, fuel rate, top gas utilization factor, top gas temperature, and liquid temperature, as well as the BF inner states such as the CZ shape and location, gas temperatures, and the ore reduction process.^[57] Second, this model gives satisfactory prediction values of the overall performance

indicators of an industrial BF.^[57] On this basis, the effects of blast rate, coke rate, oxygen enrichment, and sinter reduction degradation on BF performance have also been studied, which are still consistent with the well-established trends in field experiences.^[56,57,60] Third, the current model has also shown its capability to be used to simulate the 3D asymmetric inner states resulting from tuyere closure, and the simulated 3D asymmetric deadman profile and CZ shape variation are in good agreement with the experimental observations.^[71] However, industrial data are currently unavailable to directly validate the predicted effects of non-uniform burden distribution on BF inner states. Future efforts should be considered to overcome this problem. In this direction, various information can be considered, such as the imbalance in the signals from above-burden diagonal probes, asymmetric wall cooling losses or temperatures, and non-uniform burden descent.

B. Layer Structure and Cohesive Zone

Figure 4 initially illustrates the layered burden structure under the current simulation conditions. Four main zones inside BF, namely, lumpy zone, CZ, dripping zone, and deadman are clearly predicted. It can be seen that with increasing A_{UD} , the lumpy zone volume decreases in the low ore-to-coke region but increases in the high ore-to-coke region. It can also be seen that, with increasing A_{UD} , the gas volume fraction slightly above the CZ increases in the low ore-to-coke region but decreases in the high ore-to-coke region. This is mainly caused by the asymmetric sinter reduction degradation, which leads to the asymmetric distribution of gas volume fraction and bed permeability. The sinter size reduction degradation shown in Figures 16 and 17 will be later discussed. The deadman profile, which is largely

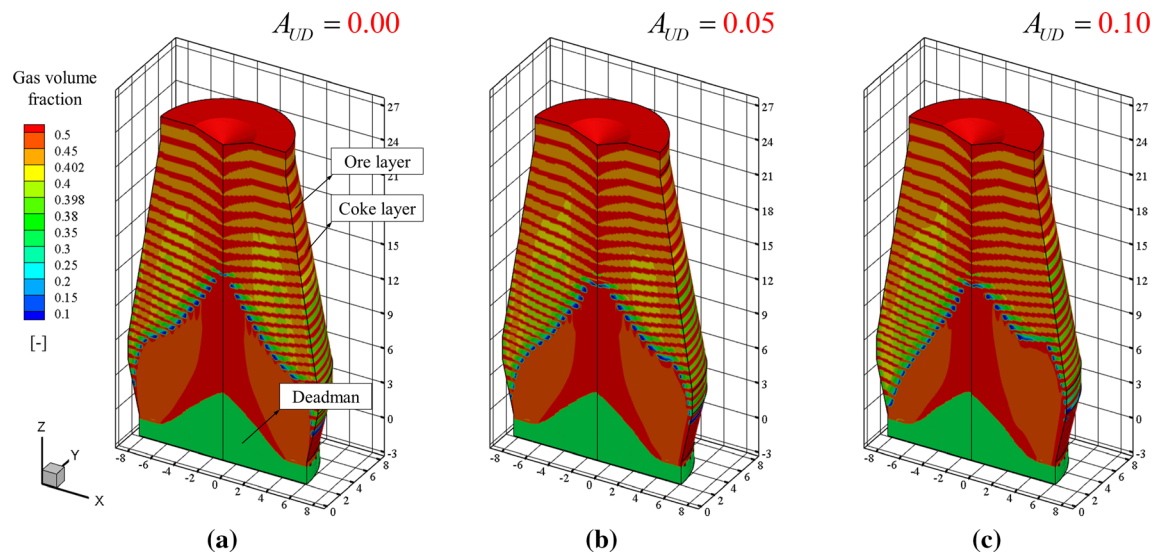


Fig. 4—Deadman profile and layered burden structure under different A_{UD} values: (a) $A_{UD} = 0.00$; (b) $A_{UD} = 0.05$; (c) $A_{UD} = 0.10$.

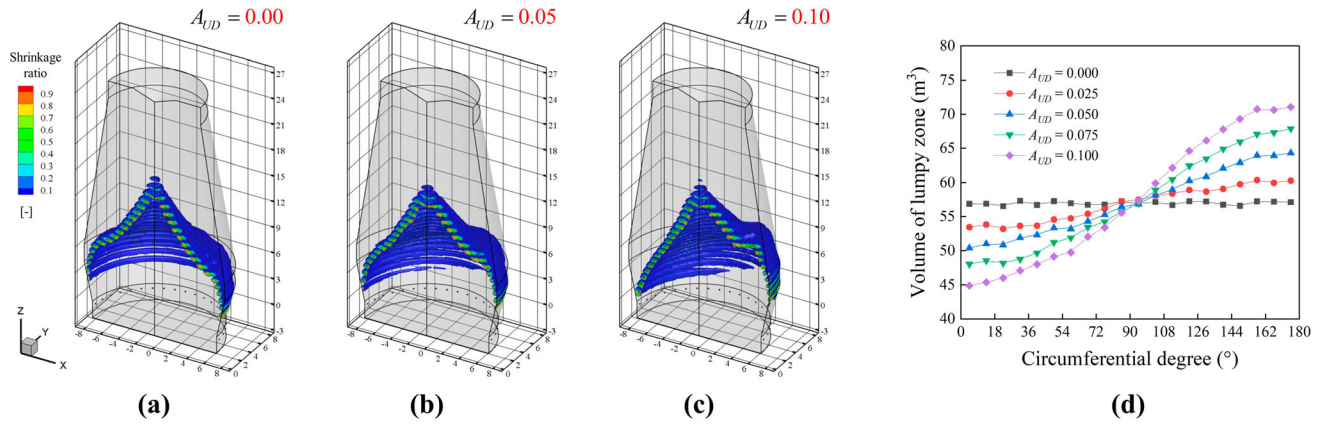


Fig. 5—CZ shape and location under different A_{UD} values [(a) $A_{UD} = 0.00$; (b) $A_{UD} = 0.05$; (c) $A_{UD} = 0.10$], and the circumferential variations of lumpy zone volume (d).

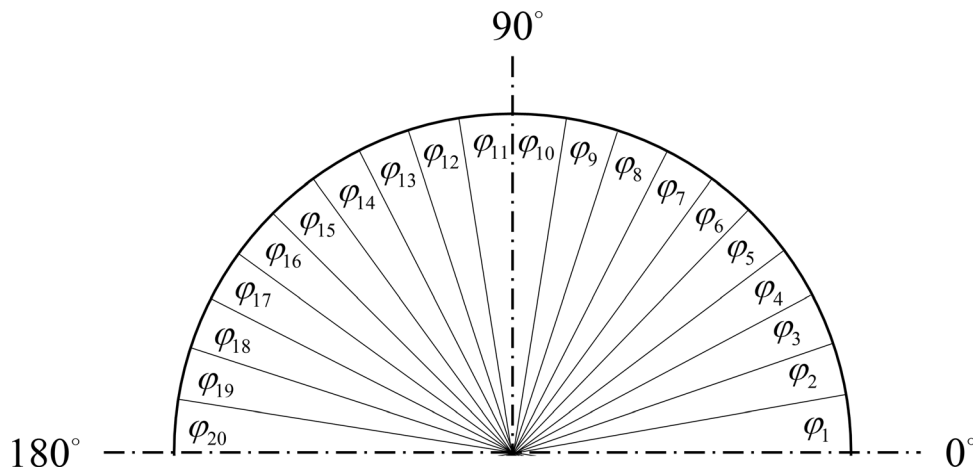


Fig. 6—Schematic illustration of sub-sectors for analyzing the circumferential non-uniformity of inner states.

determined by the solid flow in BF, does not change significantly with increasing A_{UD} . This is because the hot blast is assumed to be uniformly distributed among the 20 active tuyeres, leading to the uniform coke combustion rate that represents an important contributor to the solid flow rate. It should be noted that the predicted deadman profile is only acceptable under the current assumed uniform blast conditions. Its asymmetry will be more obvious when more realistic pressure boundary conditions are used at the tuyeres. This will also significantly affect the asymmetry of the other multiphase flow and thermochemical behaviors. However, this extended work will be continued in the future. In this study, all the simulation results are obtained and analyzed under the assumed uniform blast conditions.

The 3D CZ under different non-uniform burden distributions are also illustrated (see Figure 5) because of its significant importance to BF operation.^[2] Under uniform burden distribution, the CZ presents an “inverted-V” shape under the radial center-charged coke distribution. With increasing A_{UD} value, the CZ shape

presents different characteristics between the low and high ore-to-coke regions. In the low ore-to-coke region, the CZ position continuously rises with increasing A_{UD} . The number of CZ layer gradually decreases. The CZ layers close to the furnace wall becomes thinner; however, the fused layers in the middle of CZ become longer, which are not in favor of the stable BF operation and might deteriorate the BF states according to the previous studies.^[8] In the high ore-to-coke region, the CZ becomes much longer and steeper, and almost approaches the raceways at $A_{UD} = 0.10$. This increases the possibility of instabilities at the raceways due to the strong interactions between the intensified descending liquid flow (see Figure 13) and the high-speed injected blast. This is also influenced by the deteriorated liquid fluidity that results from the low liquid temperature in the high ore-to-coke region (see Figure 14). In general, the 3D asymmetric CZ resulted from the current non-uniform burden distribution is not in favor of the stable BF operation in both low ore-to-coke region and high ore-to-coke region when A_{UD} is relatively large. On

the other hand, the CZ top location just slightly changes and the general “inversed-V” CZ shape remains with increasing A_{UD} . For a quantitative description of the 3D asymmetric CZ position, the lumpy zone volume above each tuyere sector is plotted along the circumference [see Figure 5(d)]. Interestingly, the lumpy zone volume also presents the sine/cosine like variations along the circumference, similar to the circumferential variations of top ore-to-coke ratio [see Figure 2(c)].

C. Multiphase Flow and Thermochemical Behaviors

In this section, the asymmetric multiphase flow and thermochemical behaviors are illustrated and analyzed, represented by the gas velocity and pressure, solid temperature, liquid mass flow rate and temperature, and iron ore reduction degree. In order to quantify the

non-uniformity of different in-furnace variables at different BF heights, the parameter σ is used and calculated in Eq. (3). As shown in Figure 6, each horizontal cross section at one specific BF height is equally divided into 20 sectors, with each sector occupying a tuyere region. The average value of each specific in-furnace variable φ in sector i is firstly calculated with Eq. [(3c)], where N_i is the number of computational cells in the i th sub-sector and $\varphi_{i,k}$ denotes the considered variable on the k th cell. The standard deviation of array φ_i is used to quantify the non-uniformity of variable φ , marked as σ . Large σ demonstrates that the non-uniformity of variable φ is significant. $\sigma = 0$ demonstrates that variable φ is uniform in the circumferential direction.

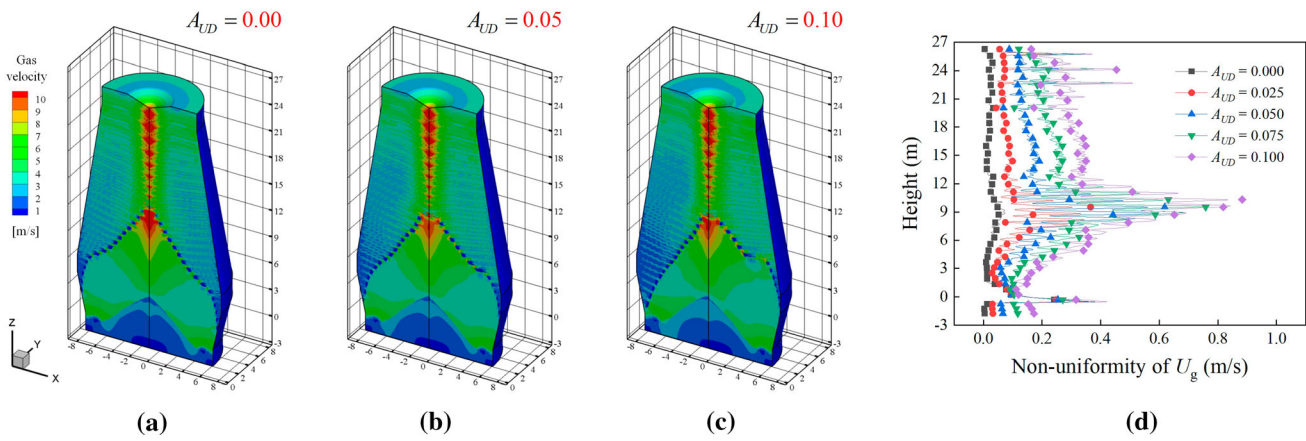


Fig. 7—Spatial distributions of gas velocity under different A_{UD} values [(a) $A_{UD} = 0.00$; (b) $A_{UD} = 0.05$; (c) $A_{UD} = 0.10$], and its non-uniformity variations along the axial direction (d).

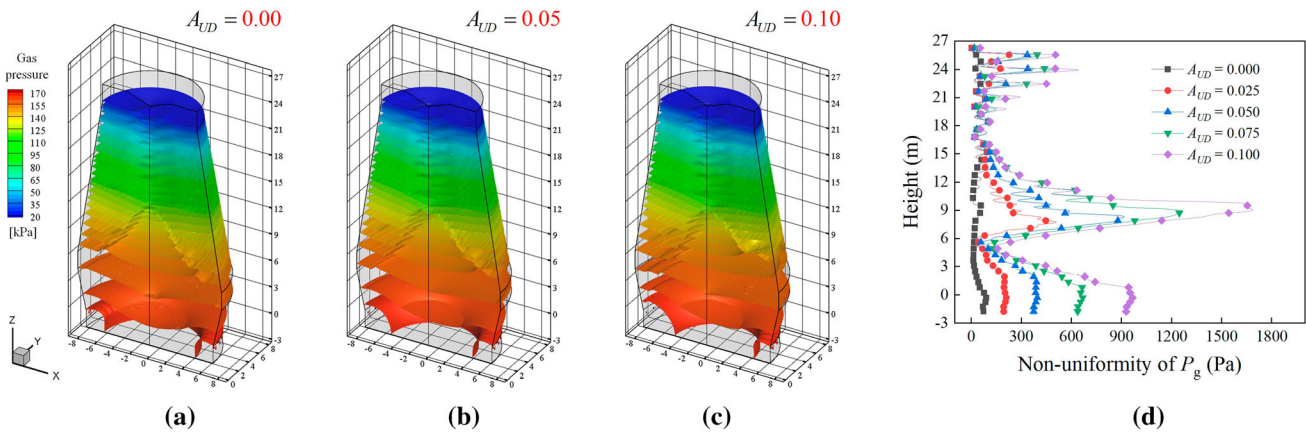


Fig. 8—Spatial distributions of gas pressure under different A_{UD} values [(a) $A_{UD} = 0.00$; (b) $A_{UD} = 0.05$; (c) $A_{UD} = 0.10$], and its non-uniformity variations along the axial direction (d).

$$\sigma = \sqrt{\frac{1}{20} \sum_{i=1}^{20} (\varphi_i - \bar{\varphi})^2}, \quad [3a]$$

$$\bar{\varphi} = \frac{1}{20} \sum_{i=1}^{20} \varphi_i, \quad [3b]$$

$$\varphi_i = \frac{1}{N_i} \sum_{k=1}^{N_i} \varphi_{i,k}. \quad [3c]$$

The spatial distributions of gas velocity and gas pressure under different non-uniform burden distributions and their non-uniformities along the BF heights are shown in Figures 7 and 8, respectively. It can be seen from Figures 7(a) through (c) that the gas velocity increases in the low ore-to-coke region but decreases in the high ore-to-coke region. Conversely, the gas pressure

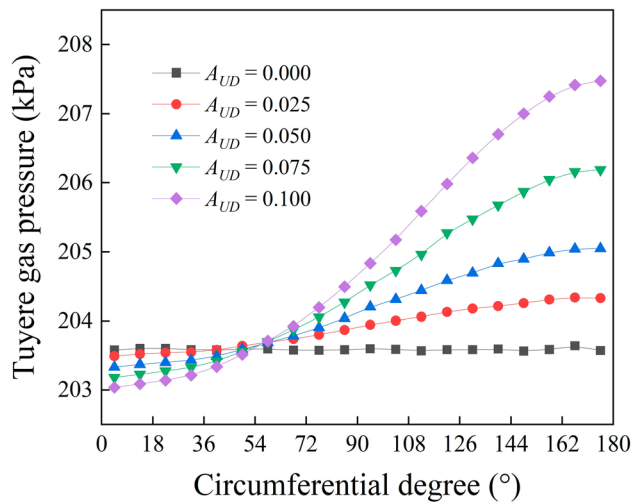


Fig. 9—Circumferential distributions of tuyere gas pressure under different A_{UD} values.

decreases in the low ore-to-coke region but increases in the high ore-to-coke region [see Figures 8(a) through (c)]. This is because the coke diameter (~ 40 mm) is larger than the ore diameter (~ 13 mm), leading to higher gas permeability in the low ore-to-coke region. The circumferential distributions of tuyere gas pressure under different non-uniform burden distributions are shown in Figure 9. It can be seen that the tuyere pressure increment in the high ore-to-coke region is more significant than its decrease in the low ore-to-coke region. This is because even though the low ore-to-coke region has good permeability, the long horizontal CZ layer there hinders the gas flow and increases the localized gas pressure gradient, resulting in the less obvious change of the tuyere pressure in the low ore-to-coke region. The gas pressure distribution reflects the circumferential non-uniform bed permeability. Figures 7(d) and 8(d) plot the axial variations of gas velocity and gas pressure non-uniformities, respectively. It is found that U_g and P_g non-uniformities almost increase linearly with the increasing A_{UD} ; however, the axial variations of them are quite different. The U_g non-uniformity is apparent at both the BF upper part and the BF lower part, while the P_g non-uniformity is significant at the BF lower part but almost disappears at the BF upper part. It can be clearly seen that both the maximum U_g and P_g non-uniformities exist at round 18 m from the BF stockline.

Figure 10 shows the spatial distributions of solid temperature under different non-uniform burden distributions and its non-uniformity along the BF height. Under uniform burden distribution [see Figure 10(a)], the solid temperature is shown as a “cone” shape at the BF upper part due to the center-charged coke distribution [see Figure 2(b)], and it is presented as an “inversed glass” shape at the BF lower part due to the lower permeability of the deadman. With increasing A_{UD} value, the temperature rises in the low ore-to-coke region and forms the “W-shape” in the BF upper part at the relatively large A_{UD} value [see Figure 10(c)] conversely, the temperature drops in the high ore-to-coke region. Under the current simulation conditions, the heat input from the furnace bottom, mainly includes the

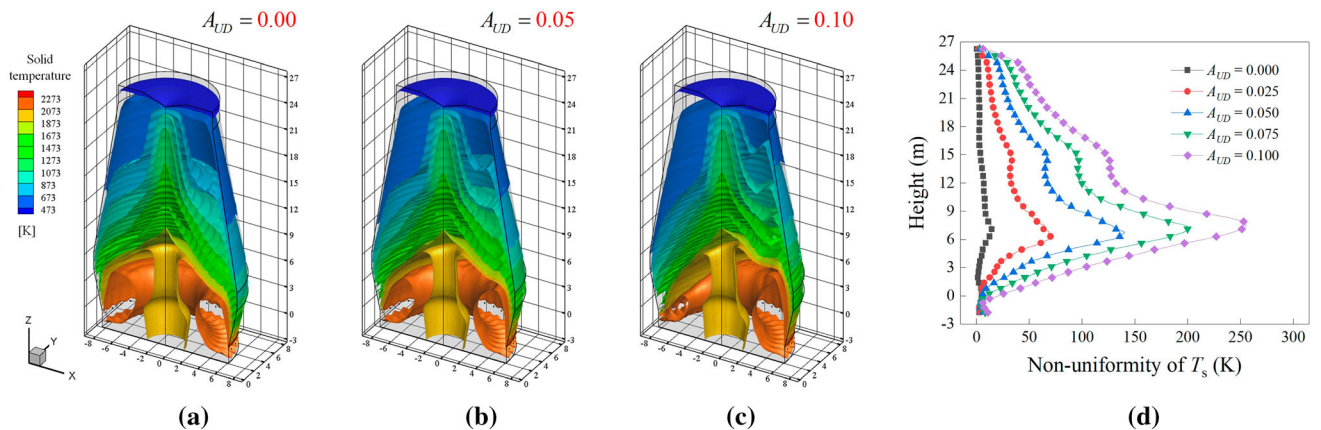


Fig. 10—Spatial distributions of solid temperature under different A_{UD} values [(a) $A_{UD} = 0.00$; (b) $A_{UD} = 0.05$; (c) $A_{UD} = 0.10$], and its non-uniformity variations along the axial direction (d).

Table VI. Heat Balance Analysis under Different Non-uniform Burden Distributions

Variables	$A_{UD} = 0.000$			$A_{UD} = 0.025$			$A_{UD} = 0.050$			$A_{UD} = 0.075$			$A_{UD} = 0.100$		
	Low	High	Low + High	Low	High	Low + High	Low	High	Low + High	Low	High	Low + High	Low	High	Low + High
Total Input	1.904	1.904	3.808	1.904	1.904	3.808	1.904	1.904	3.808	1.904	1.904	3.808	1.904	1.904	3.808
Burden	0.001	0.001	0.002	0.001	0.001	0.002	0.001	0.001	0.002	0.001	0.001	0.002	0.001	0.001	0.002
Hot Blast	0.751	0.751	1.502	0.751	0.751	1.502	0.751	0.751	1.502	0.751	0.751	1.502	0.751	0.751	1.502
Combustion	1.152	1.152	2.304	1.152	1.152	2.304	1.152	1.152	2.304	1.152	1.152	2.304	1.152	1.152	2.304
Total Output	1.904	1.904	3.808	1.901	1.907	3.808	1.897	1.911	3.808	1.893	1.915	3.808	1.89	1.918	3.808
Top Gas	0.265	0.265	0.530	0.274	0.258	0.532	0.282	0.251	0.533	0.289	0.246	0.535	0.298	0.239	0.537
Wall Heat Loss	0.164	0.164	0.328	0.174	0.155	0.329	0.195	0.135	0.330	0.204	0.128	0.332	0.211	0.123	0.334
Reactions	0.927	0.927	1.854	0.915	0.939	1.854	0.892	0.963	1.855	0.883	0.974	1.857	0.872	0.987	1.859
HM and Slag	0.548	0.548	1.096	0.538	0.555	1.093	0.528	0.562	1.09	0.517	0.567	1.084	0.509	0.569	1.078

Unit: GJ/tHM; "Low" refers to the low ore-to-coke region; and "High" refers to the high ore-to-coke region.

physical heat of hot blast and the combustion heat, is assumed to be uniformly distributed among the 20 inactive tuyeres. The non-uniform temperature distribution mainly results from the circumferential gas re-distribution at the furnace lower part and the heat consumption difference between the low ore-to-coke region and the high ore-to-coke region. Detailed analysis of the heat consumption under different non-uniform burden distributions is illustrated in Table VI. It can be seen that with increasing A_{UD} , the reaction heat consumption and liquid sensible heat in the high ore-to-coke region continuously increase, leading to an increasing total heat consumption there, even though the wall enthalpy loss and top gas enthalpy loss show the opposite trend.

Figures 11 and 12 quantitatively illustrate the circumferential non-uniformity at the furnace top, represented by the radial distributions of top gas temperature and top gas utilization factor at three circumferential degrees. It can be seen that with increasing A_{UD} values, the top gas temperature increases at $\theta = 4.5^\circ$ [see Figure 11(a)], but decreases at $\theta = 174.5^\circ$ [see Figure 11(c)]. Conversely, the top gas utilization factor decreases at $\theta = 4.5^\circ$ [see Figure 12(a)], but increases at $\theta = 174.5^\circ$ [see Figure 12(c)]. Differently, the variations of both top gas temperature and top gas utilization factor are not significant at $\theta = 90^\circ$ [see Figures 11(b) and 12(b)].

Figure 13 shows the liquid flow in the dripping zone and at the slag surface under different non-uniform burden distributions. In the current BF process model, with the combination of the force balance model and the stochastic model, the trickling flow characteristics of liquid can be effectively described, especially the re-distribution effect by the impermeable CZ and raceway boundaries.^[56,57] The liquid generated in one CZ layer accumulates and spreads on the top of the lower fused layer [Figure 13(a)]. A fraction of this liquid moves inward over the layer and combines with the liquid source generated, forming a relatively dense downward liquid flow channel at the end of flat parts of the CZ. This is the so-called "icicle" flow. The remaining fraction of liquid moves outward and flows down along cohesive layers, forming significant liquid streams at the CZ root. Because of the impermeable boundary of raceways, the liquid passes around raceways and flows down through the coke bed between raceways. It can be seen from the slag surface of the high ore-to-coke region, the liquid flow rate in the areas between raceways increases significantly with increasing A_{UD} , but decreases in the other areas of the high ore-to-coke region. This is because the CZ becomes much steeper in the high ore-to-coke region [see Figure 5(c)], and more liquid accumulates at the root of CZ due to the re-distribution effect of CZ on liquid flow. Because of the less charged ore in the low ore-to-coke region, the liquid flow rate is significantly reduced there. This liquid flow rate is also influenced by the re-distribution effect of inclined CZ, part of the liquid generated in the low ore-to-coke region flows toward the high ore-to-coke region. In addition, due to the appearance of the long horizontal CZ [see Figure 5(c)], the liquid flow

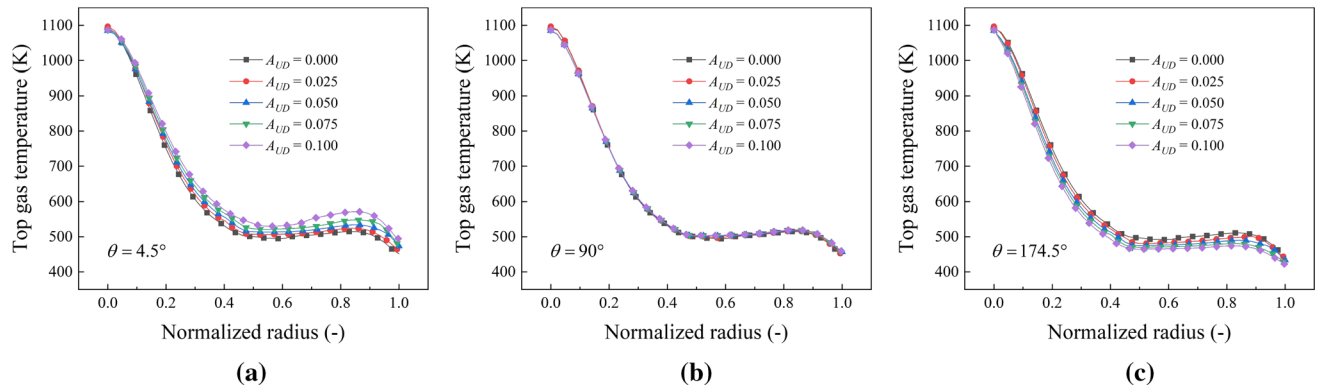


Fig. 11—Radial distributions of top gas temperature at different circumferential degrees: (a) $\theta = 4.5^\circ$; (b) $\theta = 90^\circ$; (c) $\theta = 174.5^\circ$.

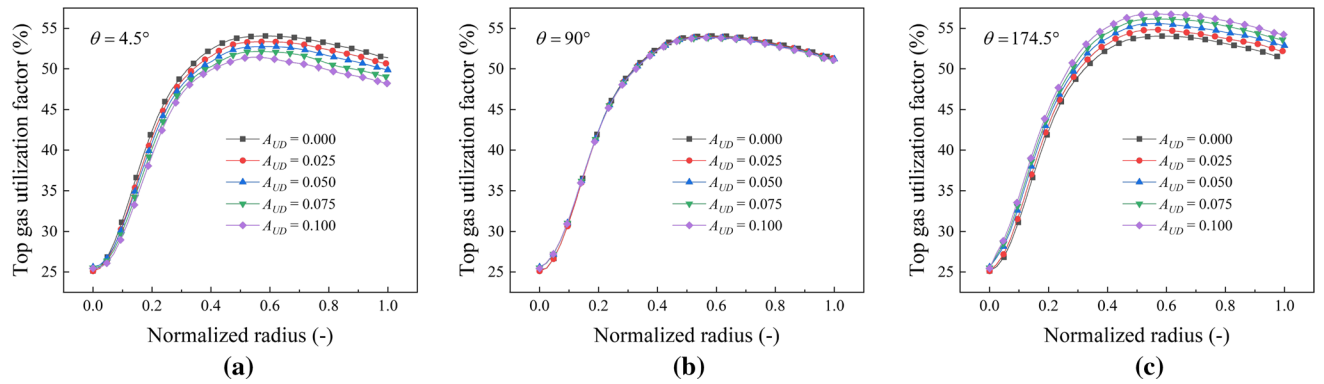


Fig. 12—Radial distributions of top gas utilization factor at different circumferential degrees: (a) $\theta = 4.5^\circ$; (b) $\theta = 90^\circ$; (c) $\theta = 174.5^\circ$.

trajectories significantly change, resulting in the strong localized liquid flow [see Figure 13(c)], reducing the gas permeability in the coke window, and increasing the localized pressure gradient [see Figure 8(c)].

Figures 14(a) through (c) shows the liquid temperature in the dripping zone and its distributions at the slag surface under different non-uniform burden distributions. The liquid temperature is shown in the form of “wrinkles” corresponding to the characteristics of trickling flow. With increasing A_{UD} values, the temperature increases in the low ore-to-coke region but decreases in the high ore-to-coke region. For quantitative analysis, the circumferential distribution of mass-averaged liquid temperature of each tuyere sector at the slag surface is plotted in Figure 14(d). It can be seen that the liquid temperature at the 20th tuyere decreases by around 6K on average with an increment of A_{UD} by 1 pct. This decreasing liquid temperature is attributed to the increasing liquid mass flow rate (see Figure 13), shortening liquid heating distance and the gas re-distribution at the lower BF, and *vice versa* in the low ore-to-coke region.

Figure 15 shows the spatial distributions of reduction degree under different non-uniform burden distributions and its non-uniformity variations along the BF height. Under uniform burden distribution [see Figure 15(a)],

the reduction degree presents the “cone” shape at the BF upper part due to the center-charged coke distribution. With increasing A_{UD} values, the reduction process of iron ore accelerates in the low ore-to-coke region, attributed to the increasing reducing gas flow rate, decreasing iron ore descending rate, and the increasing solid temperature. Conversely, the iron ore reduction process decelerates in the high ore-to-coke region. Similar to the axial variations of U_g , P_g , and T_s non-uniformities, the maximum RD uniformity still exists at round 18 m from the BF stockline.

D. Particle Size Reduction

In the current 3D BF process model, two factors are specifically considered: the sinter size reduction resulting from low-temperature reduction degradation and the coke size reduction resulting from coke gasification.^[60] Figures 16 and 18 show the spatial distributions of sinter diameter and coke diameter, respectively, under different non-uniform burden distributions. For quantitative analysis purposes, the axial variations of sinter diameter and coke diameter at the representative location of low ore-to-coke region (4.5 deg) and high ore-to-coke region (174.5 deg) are shown in Figures 17 and 19, respectively. It can be seen from Figure 16 that the sinter size

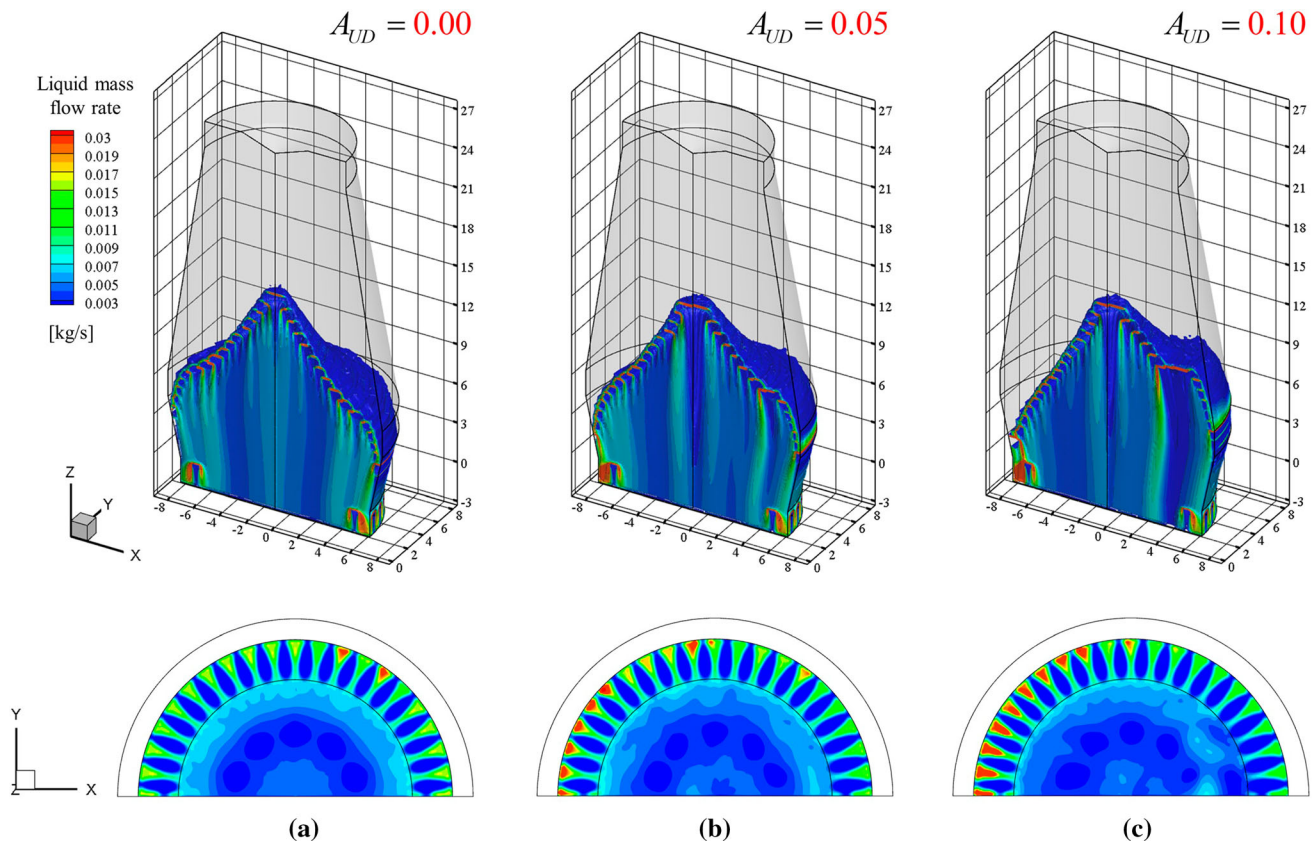


Fig. 13—Spatial distributions of liquid mass flow rate (upper row) in the dripping zone and at the slag surface (lower row) under different A_{UD} values: (a) $A_{UD} = 0.00$; (b) $A_{UD} = 0.05$; (c) $A_{UD} = 0.10$.

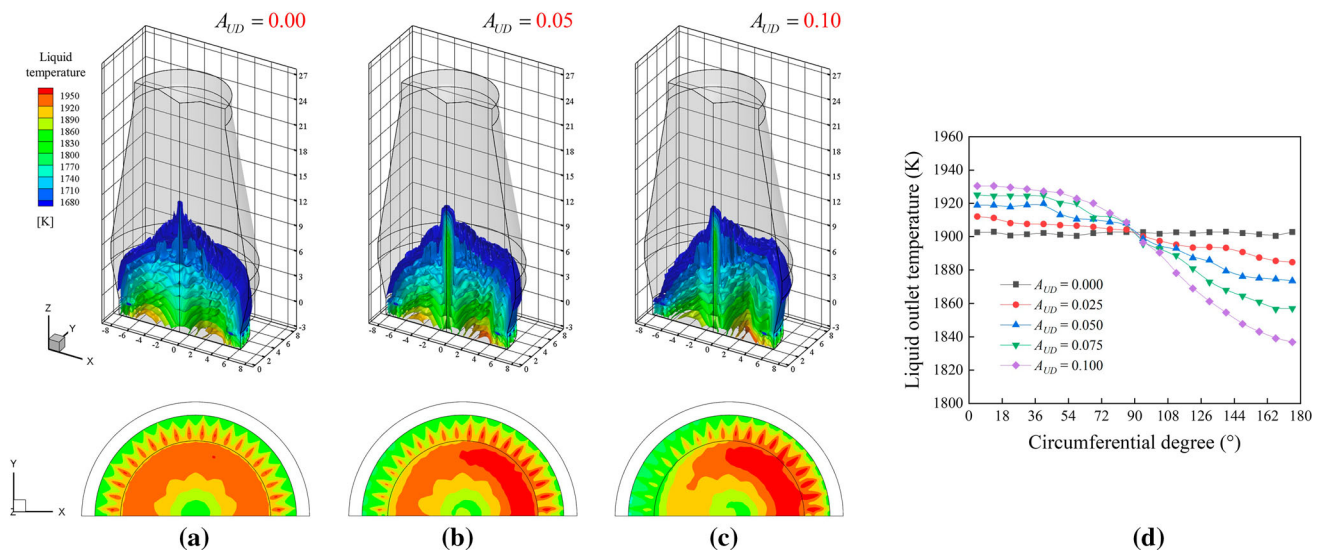


Fig. 14—Spatial distributions of liquid temperature (upper row) in the dripping zone and at the slag surface (lower row) under different A_{UD} values [(a) $A_{UD} = 0.00$; (b) $A_{UD} = 0.05$; (c) $A_{UD} = 0.10$] and the circumferential distributions of liquid temperature at the slag surface (d).

degradation mainly occurs in the BF upper zone that is close to the furnace periphery. With increasing A_{UD} values, the sinter size before entering CZ increases in the low ore-to-coke region [see Figure 17(a)] but decreases in the high ore-to-coke region [see Figure 17(b)]. For

coke particles, it can be seen from Figure 18 that the region where the coke size reduction happens massively shifts down when compared with sinter size degradation. With increasing A_{UD} values, the coke size entering the raceway increases in the low ore-to-coke region [see

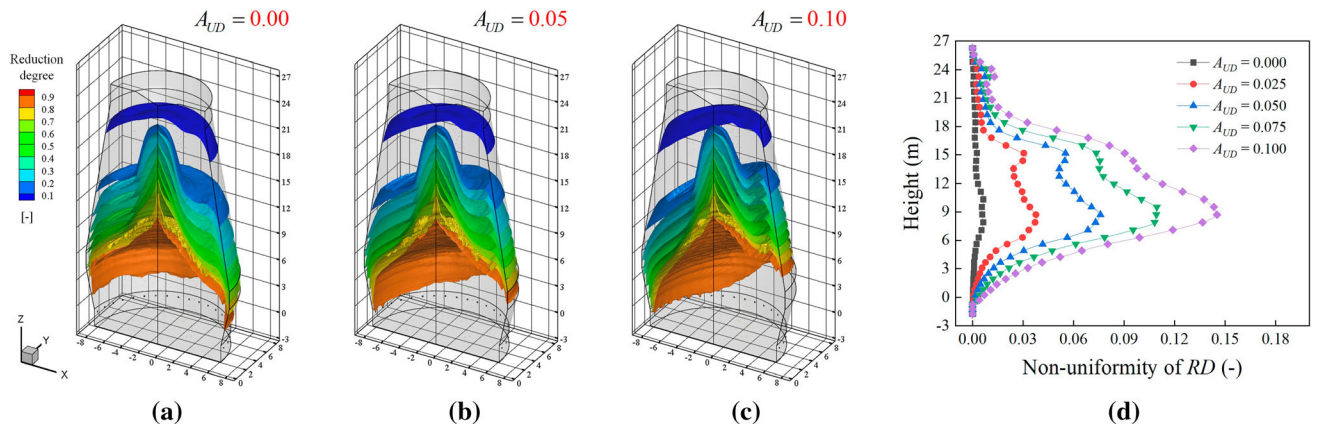


Fig. 15—Spatial distributions of reduction degree under different A_{UD} values [(a) $A_{UD} = 0.00$; (b) $A_{UD} = 0.05$; (c) $A_{UD} = 0.10$], and its non-uniformity variations along the axial direction (d).

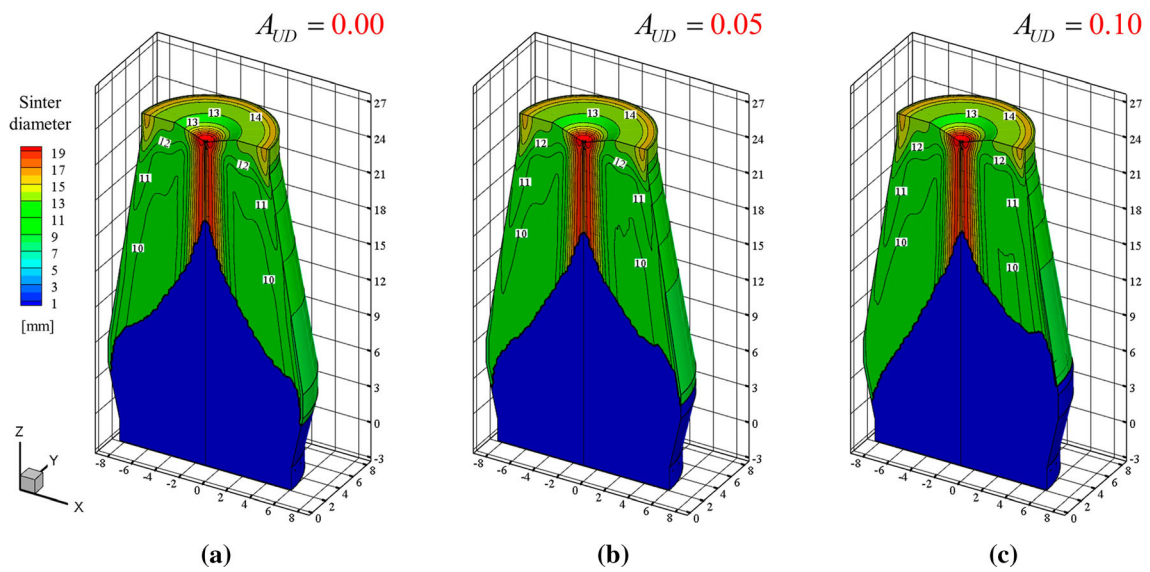


Fig. 16—Spatial distributions of sinter diameter under different A_{UD} values: (a) $A_{UD} = 0.00$; (b) $A_{UD} = 0.05$; (c) $A_{UD} = 0.10$.

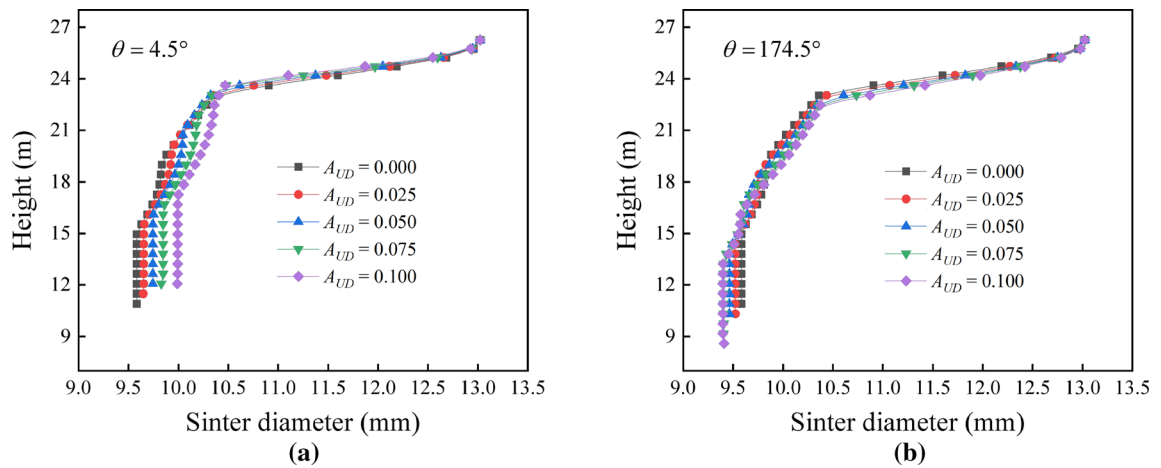


Fig. 17—Axial variations of sinter diameter at the representative location of (a) low ore-to-coke region and (b) high ore-to-coke region.

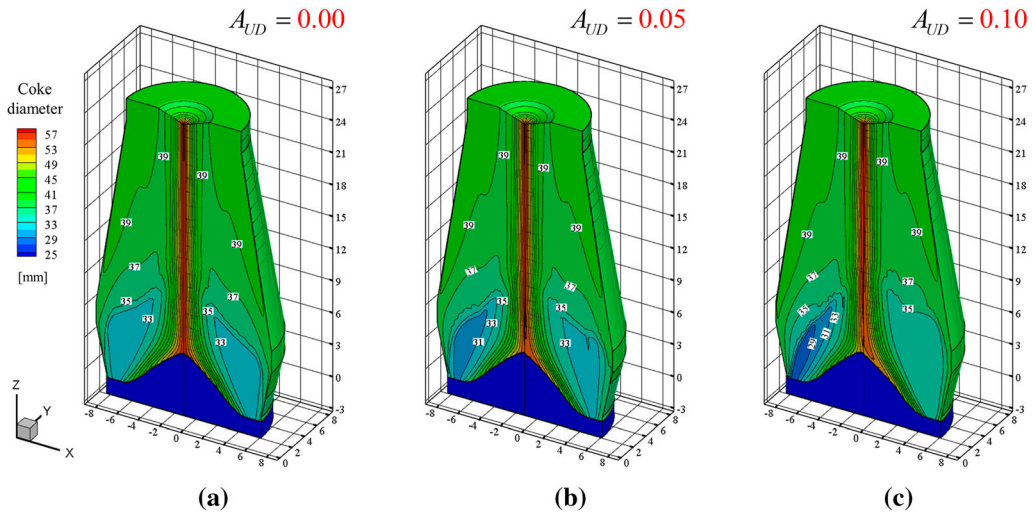


Fig. 18—Spatial distributions of coke diameter under different A_{UD} values: (a) $A_{UD} = 0.00$; (b) $A_{UD} = 0.05$; (c) $A_{UD} = 0.10$.

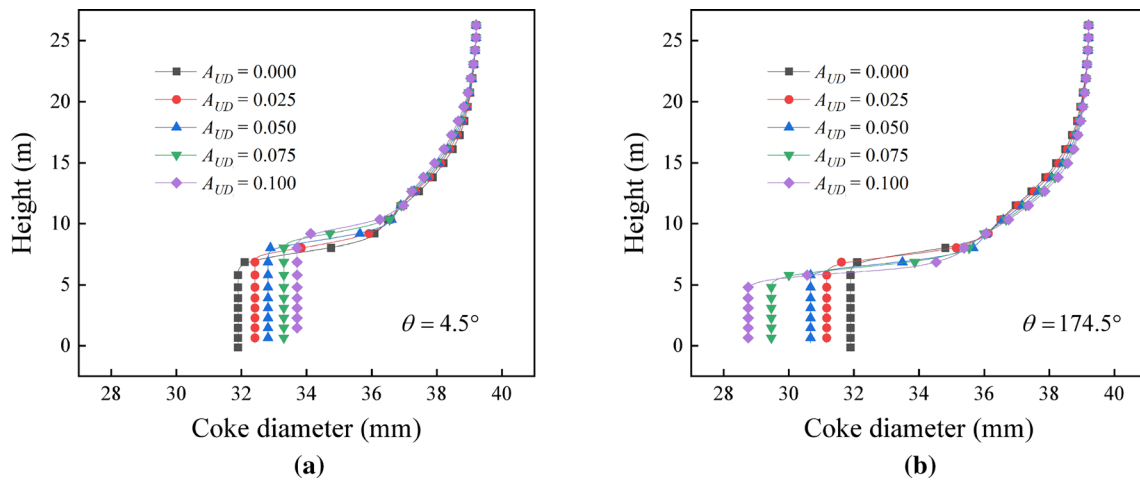


Fig. 19—Axial variations of coke diameter at the representative location of (a) low ore-to-coke region and (b) high ore-to-coke region.

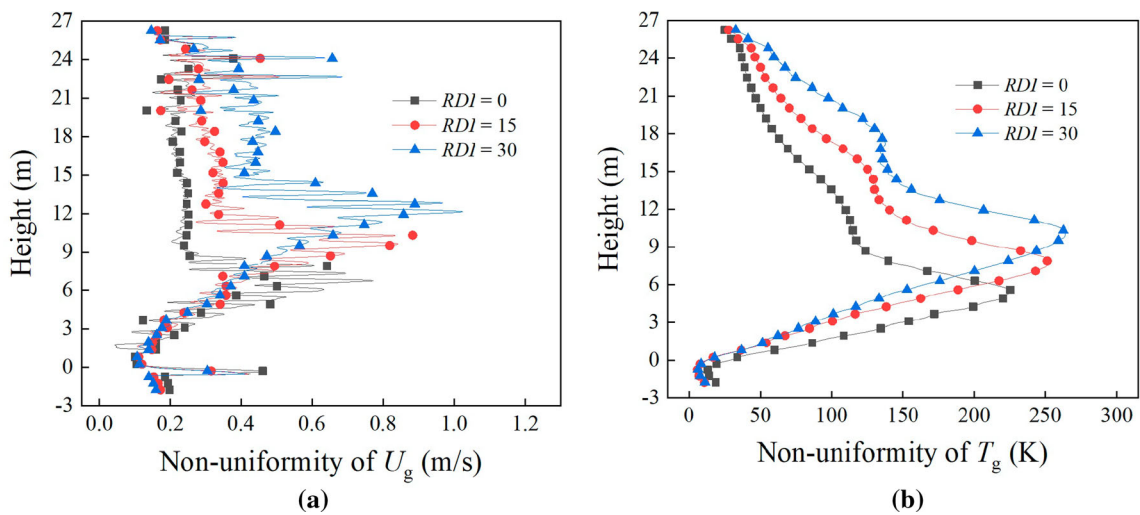


Fig. 20—Effect of RDI on the non-uniformity variations of representative in-furnace states at $A_{UD} = 0.10$: (a) gas velocity, (b) gas temperature.

Table VII. Overall Performance Indicators Under Different Non-uniform Burden Distributions

Variables	$A_{UD} = 0.000$	$A_{UD} = 0.025$	$A_{UD} = 0.050$	$A_{UD} = 0.075$	$A_{UD} = 0.100$
Blast Rate (BR), Nm ³ /s	120	120	120	120	120
Coke Rate (CR), kg/tHM	300	300	300	300	300
PCI Rate (PR), kg/tHM	185	185	185	185	185
Productivity (P), tHM/m ³ /day	2.180	2.180	2.180	2.180	2.180
Average Tuyere Gas Pressure (TGP), kPa	203.47	203.79	204.32	204.70	204.83
Average Top Gas Utilization Factor (TGUF), Pct	51.69	51.65	51.66	51.67	51.66
Average Top Gas Temperature (TGT), K (°C)	533.62 (260.47)	534.19 (261.04)	534.59 (261.44)	535.05 (261.9)	536.01 (262.86)
Average Liquid Outlet Temperature (LT), K (°C)	1901.22 (1628.07)	1899.04 (1625.89)	1897.93 (1624.78)	1894.78 (1621.63)	1889.43 (1616.28)

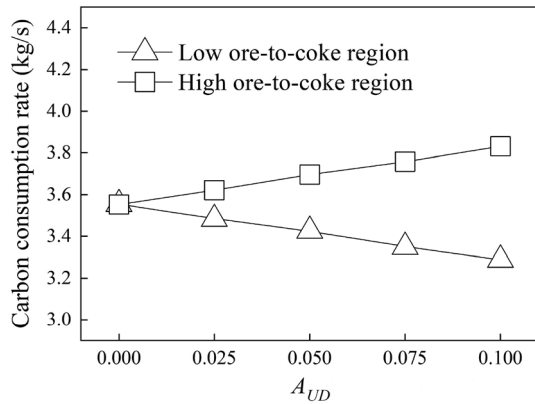


Fig. 21—Comparison of the carbon consumption rate between the low ore-to-coke region and the high ore-to-coke region under different A_{UD} values.

Figure 19(a)] but decreases in the high ore-to-coke region [see Figure 19(b)]. In general, both the sinter size degradation and coke size reduction become much severe in the high ore-to-coke region at large A_{UD} value, leading to much more deteriorated bed permeability there. Conversely, much better bed permeability is obtained in the low ore-to-coke region. This intensified asymmetric characteristic of bed permeability caused by sinter and coke size reduction affects the gas flow re-distribution and further affects the other thermochemical behaviors, such as the above-mentioned gas pressure, solid temperature, liquid temperature, *etc.*

In order to quantify the effects of sinter sizes reduction on the non-uniformity of BF in-furnace states, simulations are carried out under different sinter reduction degradation index (RDI) values, namely $RDI = 0, 15, \text{ and } 30$. Figure 20 specifically illustrates the non-uniformity variations of representative in-furnace states at $A_{UD} = 0.10$, including gas velocity and gas temperature. It can be seen that with increasing RDI, the peak non-uniformities of the two illustrated in-furnace variables continuously increases. This proves that the sinter size reduction resulting from low-temperature reduction degradation can intensify the internal asymmetric distribution of BF inner states under non-uniform burden distribution. As a result, special

attention should be paid to the burden-charging non-uniformity when the sinter RDI is large in real BF operations.

E. Overall BF Performance

In addition to the asymmetric inner states, the overall performance indicators are also analyzed under different non-uniform burden distributions, as shown in Table VII. It is noted that the average tuyere gas pressure is the average value of the 20 active tuyeres, and the average top gas utilization factor, average top gas temperature, and average liquid temperature are also the respective average values at the furnace throat or the slag surface. It can be seen from Table VII that, compared with the asymmetric internal states, the variation of overall BF performance is not significant. This is because the high ore-to-coke region and the low ore-to-coke region cancel each other. Taking carbon consumption as an example (see Figure 21), with increasing A_{UD} , the total carbon consumption rate by direct reduction and solution loss increases in the high ore-to-coke region but decreases in the low ore-to-coke region, leading to the fluctuating average gas utilization factor at the furnace top (see Table VII). At the same time, the heat loss by the top gas dissipation increases in the low ore-to-coke region. Still, it decreases in the high ore-to-coke region. These together result in a slightly increased average gas temperature at the furnace top. In addition, the tuyere gas pressure decreases in the low ore-to-coke region but increases in the high ore-to-coke region (see Figure 9), leading to a slightly increased average gas pressure at the tuyere. The average liquid outlet temperature decreases by around 12 K when A_{UD} increases from 0.0 to 0.1, which indicates that the coke rate needs to be increased to supplement extra thermal energy to heat the melting slag and HM to the required temperature.

Even though the average overall global performance indicators change slightly with respect to the non-uniform burden distribution, it does not indicate that the BF running status under non-uniform burden distribution is the same as that under uniform case. The evaluation of BF behaviors is also related to the complicated inner states. One representative example of this is the non-uniform distributions of liquid flow

and temperature. Even though the average liquid outlet temperature changes slightly, in order to comprehensively evaluate the BF running status, the liquid flow and temperature in the hearth should be further investigated in the future. On the other hand, the results in this work are simulated under constant blast rate. Even though the value opening in front of each tuyere could be adjusted in order to ensure the uniform gas supply, the tuyere gas pressure variation may lead to the variation of total blast rate. This is another reason why the average overall global performance change slightly.

IV. CONCLUSIONS

The effect of circumferential non-uniform burden distribution on the 3D asymmetric inner states and the overall performance of BF has been comprehensively studied under uniform gas supply to tuyeres. This is based on a 5000-m³ industrial BF and realized by using the recently developed 3D steady-state BF process model. The multiphase flow and thermochemical behaviors between the high ore-to-coke region and the low ore-to-coke region are compared and illustrated. The major findings of this work are summarized as follows:

- (1) The high ore-to-coke region has thicker ore layer, thinner coke layer, and thus poorer permeability; on the contrary, the low ore-to-coke region has thinner ore layer, thicker coke layer, and better permeability. Therefore, the assumed uniform hot reducing gas is re-distributed in the BF shaft, and more gas flows from the high ore-to-coke region to low ore-to-coke region, which raises the CZ position in the low ore-to-coke region. On the contrary, the CZ in the high ore-to-coke region becomes much steeper, thicker and longer, with its root almost approaching the raceways.
- (2) The changes of CZ shape under non-uniform burden distributions also exert significant influence on the gas pressure drop and liquid flow. Because of the re-distribution effect of impermeable CZ layers on the liquid flow, the liquid flow rate at the CZ root in the high ore-to-coke region dramatically increases, which reduces the permeability of the coke bed in front of the tuyeres. In the low ore-to-coke region, the long horizontal CZ layer increases the localized gas pressure gradient and forms the localized strong “trickling” liquid flow, which do not promote the stability of BF operation according to observations from real BFs. From the perspective of multiphase thermochemical behaviors, the thermal state becomes better and the reduction process accelerates in the low ore-to-coke region, and the opposite effect is observed in the high ore-to-coke region.
- (3) Under non-uniform burden distribution, both the sinter size reduction resulting from low-temperature reduction degradation and the coke size reduction resulting from coke gasification become more severe in the high ore-to-coke region; however, both of

them slow down in the low ore-to-coke region. This asymmetric particle size distribution intensifies the asymmetric distributions of BF inner states, which is especially true at large sinter RDI values. Therefore, special attention should be paid to the burden-charging non-uniformity when sinter RDI is relatively large.

- (4) Due to the mutual offset between the high and low ore-to-coke regions, the global performance indicators do not vary significantly. Specifically, with the increase of circumferential non-uniform degree of ore-to-coke ratio (A_{UD}), the average top gas temperature and average tuyere gas pressure slightly increase; however, the average liquid outlet temperature slightly decreases. These insignificant variations can also be attributed to the constant blast rate assumed in simulations.

Finally, it should be pointed out that the above results are obtained assuming the blast rate is uniform among the 20 active tuyeres in spite of their asymmetric bed permeability. In the future, in order to predict the asymmetric inner states more realistically, the pressure boundary conditions will be implemented at the tuyeres in the model. This study will also be extended to consider the local asymmetry, *e.g.*, caused by the dense bird’s nest of some tuyeres. In addition, in order to comprehensively evaluate the BF running status under non-uniform burden distribution, an integrated BF model that covers the BF shaft and hearth should be helpful. This will be done in our future work.

ACKNOWLEDGMENTS

The authors are grateful to the Baosteel Australia Research and Development Center (BAJC) (BA16002), the National Natural Science Foundation of China (52034003), and Natural Science Foundation of Jiangsu Province (BK20210007) for the financial support of this work, and the National Computational Infrastructure (NCI) for the use of high-performance computational facilities, and *CAFFA3D* for making a useful code available for free use and adaptation.

CONFLICT OF INTEREST

On behalf of all authors, the corresponding author states that there is no conflict of interest.

ABBREVIATIONS

a_{FeO}	The activity of molten wustite
A_c	Effective surface area of coke for reaction, m ²
A_{UD}	Circumferential non-uniform degree of ore-to-coke ratio
BF	Blast furnace

SUPERSCRIPTS

e Effective
 g Gas
 l Liquid
 s Solid
 T Transpose

REFERENCES

1. M. Geerdes, R. Chaigneau, and O. Lingardi: *Modern Blast Furnace Ironmaking: An Introduction*, Ios Press, Amsterdam, 2020.
2. Y. Omori: *Blast Furnace Phenomena and Modelling*, Elsevier Science Pub. Co., Inc., New York, 1987.
3. J. Chen, H. Zuo, Q. Xue, and J. Wang: *Powder Technol.*, 2021, vol. 398, p. 117055.
4. Y. Xu, J. Xu, C. Sun, K. Ma, C. Shan, L. Wen, S. Zhang, and C. Bai: *Powder Technol.*, 2018, vol. 328, pp. 245–55.
5. H. Mio, S. Komatsuki, M. Akashi, A. Shimosaka, Y. Shirakawa, J. Hidaka, M. Kadowaki, S. Matsuzaki, and K. Kunitomo: *ISIJ Int.*, 2009, vol. 49, pp. 479–86.
6. Z.Y. Zhou, H.P. Zhu, B. Wright, A.B. Yu, and P. Zulli: *Powder Technol.*, 2011, vol. 208, pp. 72–85.
7. M. Kou, S. Wu, H. Zhou, Y. Yu, and J. Xu: *ISIJ Int.*, 2018, vol. 58, pp. 2018–24.
8. Z.Y. Li, S.B. Kuang, S.D. Liu, J.Q. Gan, A.B. Yu, Y.T. Li, and X.M. Mao: *Powder Technol.*, 2019, vol. 353, pp. 385–97.
9. Y. Niwa, T. Sumigama, A. Maki, H. Ito, H. Inoue, and T. Tamura: *ISIJ Int.*, 1991, vol. 31, pp. 487–93.
10. H. Takahashi, H. Kawai, M. Kobayashi, and T. Fukui: *ISIJ Int.*, 2005, vol. 45, pp. 1386–95.
11. M. Chu, H. Nogami, and J.-I. Yagi: *ISIJ Int.*, 2004, vol. 44, pp. 510–17.
12. H. Tanaka and T. Harada: *Tetsu-to-Hagané*, 2006, vol. 92, pp. 1022–28.
13. Y. Ujisawa, K. Sunahara, Y. Matsukura, K. Nakano, and T. Yamamoto: *Tetsu-to-Hagané*, 2006, vol. 92, pp. 591–600.
14. M. Chu, Z. Liu, Z. Wang, and J.I. Yagi: *Steel Res. Int.*, 2011, vol. 82, pp. 521–28.
15. E.A. Mousa, A. Babich, and D. Senk: *ISIJ Int.*, 2011, vol. 51, pp. 350–58.
16. X.B. Yu and Y.S. Shen: *Energy Fuel*, 2019, vol. 33, pp. 11603–16.
17. Y. Liu, *Iron Steel*, 1993, vol. 4, pp. 5–10.
18. X. Huang, Q. Zheng, A. Yu, and W. Yan: *Powder Technol.*, 2021, vol. 377, pp. 350–60.
19. J. Qiu, D. Ju, J. Zhang, and Y. Xu: *Powder Technol.*, 2017, vol. 314, pp. 218–31.
20. M. Nomura, S. Taguchi, and M. Kondoh: *J. Iron Steel I. Jpn.*, 1982, vol. 68, p. 38.
21. M. Nomura, S. Taguchi, N. Tsuchiya, H. Sakimura and K. Tanaka, In *Ironm. Conf. Proc.*, (1984), pp 111-17.
22. J. Xu, S.L. Wu, M.Y. Kou, L.H. Zhang, and X.B. Yu: *Appl. Math. Model.*, 2011, vol. 35, pp. 1439–55.
23. G.L. Zhao, S.S. Cheng, W.X. Xu, and C. Li: *ISIJ Int.*, 2015, vol. 55, pp. 2566–75.
24. H.T. Zhao, M.H. Zhu, P. Du, S. Taguchi, and H.C. Wei: *ISIJ Int.*, 2012, vol. 52, pp. 2177–85.
25. T.Z. Ren, X. Jin, H.Y. Ben, and C.Z. Yu: *J. Iron Steel Res. Int.*, 2006, vol. 13, pp. 14–17.
26. S. Watakabe, K. Miyagawa, S. Matsuzaki, T. Inada, Y. Tomita, K. Saito, M. Osame, P. Sikström, L.S. Ökvist, and J.-O. Wikstrom: *ISIJ Int.*, 2013, vol. 53, pp. 2065–71.
27. J. Yagi: *ISIJ Int.*, 1993, vol. 33, pp. 619–39.
28. X.F. Dong, A.B. Yu, J. Yagi, and P. Zulli: *ISIJ Int.*, 2007, vol. 47, pp. 1553–70.
29. S. Ueda, S. Natsui, H. Nogami, J.-I. Yagi, and T. Ariyama: *ISIJ Int.*, 2010, vol. 50, pp. 914–23.
30. T. Ariyama, S. Natsui, T. Kon, S. Ueda, S. Kikuchi, and H. Nogami: *ISIJ Int.*, 2014, vol. 54, pp. 1457–71.
31. S. Ghosh, N.N. Viswanathan, and N.B. Ballal: *Steel Res. Int.*, 2017, vol. 88, p. 1600440.
32. S.B. Kuang, Z.Y. Li, and A.B. Yu: *Steel Res. Int.*, 2018, vol. 89, p. 1700071.
33. B. Xu, A. Yu, S. Chew, and P. Zulli: *Powder Technol.*, 2000, vol. 109, pp. 13–26.
34. H. Nogami, H. Yamaoka, and K. Takatani: *ISIJ Int.*, 2004, vol. 44, pp. 2150–58.
35. S. Sarkar, G.S. Gupta, and S.-Y. Kitamura: *ISIJ Int.*, 2007, vol. 47, pp. 1738–44.
36. Y. Shen, B.-Y. Guo, A. Yu, P.R. Austin, and P. Zulli: *Fuel*, 2011, vol. 90, pp. 728–38.
37. B. Guo, D. Maldonado, P. Zulli, and A. Yu: *ISIJ Int.*, 2008, vol. 48, pp. 1676–85.
38. L. Shao and H. Saxen: *Steel Res. Int.*, 2012, vol. 83, pp. 197–204.
39. L. Shao and H. Saxen: *Ind. Eng. Chem. Res.*, 2013, vol. 52, pp. 5479–488.
40. L. Shao and H. Saxen: *ISIJ Int.*, 2013, vol. 53, pp. 1756–62.
41. L. Shao and H. Saxen: *ISIJ Int.*, 2013, vol. 53, pp. 988–94.
42. H. Mio, M. Kadowaki, S. Matsuzaki, and K. Kunitomo: *Miner. Eng.*, 2012, vol. 33, pp. 27–33.
43. T. Mitra and H. Saxén, *ISIJ Int.*, 2016, pp. ISIINT-2016-114.
44. S.D. Liu, Z.Y. Zhou, K.J. Dong, A.B. Yu, D. Pinson, and J. Tsalapatis: *Steel Res. Int.*, 2015, vol. 86, pp. 651–61.
45. P.R. Austin, H. Nogami, and J. Yagi: *ISIJ Int.*, 1997, vol. 37, pp. 458–67.
46. P.R. Austin, H. Nogami, and J. Yagi: *ISIJ Int.*, 1997, vol. 37, pp. 748–55.
47. K. Takatani, T. Inada, and Y. Ujisawa: *ISIJ Int.*, 1999, vol. 39, pp. 15–22.
48. J.A. de Castro, H. Nogami, and J. Yagi: *ISIJ Int.*, 2002, vol. 42, pp. 44–52.
49. X.F. Dong, A.B. Yu, S.J. Chew, and P. Zulli: *Metall. Mater. Trans. B*, 2010, vol. 41B, pp. 330–49.
50. K. Yang, S. Choi, J. Chung, and J. Yagi: *ISIJ Int.*, 2010, vol. 50, pp. 972–80.
51. J.A. de Castro, A.J. da Silva, Y. Sasaki, and J. Yagi: *ISIJ Int.*, 2011, vol. 51, pp. 748–58.
52. D. Fu, Y. Chen, Y.F. Zhao, J. D'Alessio, K.J. Ferron, and C.Q. Zhou: *Appl. Therm. Eng.*, 2014, vol. 66, pp. 298–308.
53. S.B. Kuang, Z.Y. Li, D.L. Yan, Y.H. Qi, and A.B. Yu: *Miner. Eng.*, 2014, vol. 63, pp. 45–56.
54. Y.S. Shen, B.Y. Guo, S. Chew, P. Austin, and A.B. Yu: *Metall. Mater. Trans. B*, 2015, vol. 46B, pp. 432–48.
55. P. Zhou, H.L. Li, P.Y. Shi, and C.Q. Zhou: *Appl. Therm. Eng.*, 2016, vol. 95, pp. 296–302.
56. L.L. Jiao: *Chemical Engineering*, Monash University, Melbourne, 2020.
57. L.L. Jiao, S.B. Kuang, A.B. Yu, Y.T. Li, X.M. Mao, and H. Xu: *Metall. Mater. Trans. B*, 2020, vol. 51B, pp. 258–75.
58. S.J. Zhang, A.B. Yu, P. Zulli, B. Wright, and U. Tüzün: *ISIJ Int.*, 1998, vol. 38, pp. 1311–19.
59. Z.Y. Zhou, A.B. Yu, and P. Zulli: *Prog. Cmput. Fluid Dyn.*, 2004, vol. 4, pp. 39–45.
60. L.L. Jiao, S.B. Kuang, L.L. Liu, A.B. Yu, Y.T. Li, X.M. Mao, and H. Xu: *Metall. Mater. Trans. B*, 2021, vol. 52B, pp. 138–55.
61. T. Kon, S. Natsui, S. Ueda, and H. Nogami: *ISIJ Int.*, 2015, vol. 55, pp. 1284–90.
62. S. Natsui, A. Sawada, K. Terui, Y. Kashihara, T. Kikuchi, and R.O. Suzuki: *Chem. Eng. Sci.*, 2018, vol. 175, pp. 25–39.
63. S. Ergun: *Ind. Eng. Chem.*, 1953, vol. 45, pp. 477–85.
64. G.X. Wang, S.J. Chew, A.B. Yu, and P. Zulli: *Metall. Mater. Trans. B*, 1997, vol. 28B, pp. 333–43.
65. W. Ranz and W. Marshall: *Prog.*, 1952, vol. 48, p. 173.
66. T. Akiyama, R. Takahashi, and J. Yagi: *ISIJ Int.*, 1993, vol. 33, pp. 703–10.
67. P. Mackey and N. Warner: *Metall. Mater. Trans. B*, 1972, vol. 3B, pp. 1807–16.
68. C. Rhie and W.L. Chow: *AIAA J.*, 1983, vol. 21, pp. 1525–32.

69. S. Patankar: *Numerical Heat Transfer and Fluid Flow*, Taylor & Francis, New York, 2018.
70. G. Usera, A. Vernet, and J. Ferré: *Flow Turbul. Combust.*, 2008, vol. 81, p. 471.
71. L.L. Jiao, S.B. Kuang, Y.T. Li, X.M. Mao, H. Xu, and A.B. Yu: *Metall. Mater. Trans. B*, 2021, vol. 52B, pp. 2642–58.
72. I. Muchi: *T. Iron Steel I. Jpn.*, 1967, vol. 7, pp. 223–37.

Publisher's Note Springer Nature remains neutral with regard to jurisdictional claims in published maps and institutional affiliations.

Springer Nature or its licensor (e.g. a society or other partner) holds exclusive rights to this article under a publishing agreement with the author(s) or other rightsholder(s); author self-archiving of the accepted manuscript version of this article is solely governed by the terms of such publishing agreement and applicable law.